Biophysical Journal

Article

Biophysical Society

Compartmentalization with nuclear landmarks yields random, yet precise, genome organization

Kartik Kamat,[1] Zhuohan Lao,[1] Yifeng Qi,[1] Yuchuan Wang,[2] Jian Ma,[2] and Bin Zhang[1,*]
[1]Department of Chemistry, Massachusetts Institute of Technology, Cambridge, Massachusetts and [2]Computational Biology Department, School of Computer Science, Carnegie Mellon University, Pittsburgh, Pennsylvania

ABSTRACT The 3D organization of eukaryotic genomes plays an important role in genome function. While significant progress has been made in deciphering the folding mechanisms of individual chromosomes, the principles of the dynamic large-scale spatial arrangement of all chromosomes inside the nucleus are poorly understood. We use polymer simulations to model the diploid human genome compartmentalization relative to nuclear bodies such as nuclear lamina, nucleoli, and speckles. We show that a self-organization process based on a cophase separation between chromosomes and nuclear bodies can capture various features of genome organization, including the formation of chromosome territories, phase separation of A/B compartments, and the liquid property of nuclear bodies. The simulated 3D structures quantitatively reproduce both sequencing-based genomic mapping and imaging assays that probe chromatin interaction with nuclear bodies. Importantly, our model captures the heterogeneous distribution of chromosome positioning across cells while simultaneously producing well-defined distances between active chromatin and nuclear speckles. Such heterogeneity and preciseness of genome organization can coexist due to the nonspecificity of phase separation and the slow chromosome dynamics. Together, our work reveals that the cophase separation provides a robust mechanism for us to produce functionally important 3D contacts without requiring thermodynamic equilibration that can be difficult to achieve.

SIGNIFICANCE Microphase separation between euchromatin and heterochromatin has been proposed as a mechanism for genome compartmentalization. Such block copolymer-based models do not explicitly consider the impact of nuclear bodies. They cannot explain the remarkable observations on the precise distances between active genes and nuclear speckles. The preciseness is particularly puzzling considering the heterogeneous chromosome positions that vary significantly across cells. It is inherently inconsistent with liquid models that describe the nuclear environment as homogeneous and dynamic with propensity for significant distance variations. We carried out whole-nucleus simulations to reconcile various experimental observations and elucidate the principles of genome organization. Our simulations highlight the significance of accounting for nuclear landmarks for studying genome structure and dynamics.

INTRODUCTION

Growing evidence has demonstrated that the 3D organization of eukaryotic genomes plays essential roles in DNA-templated processes (1–10). Specifically, advancements in high-throughput sequencing and microscopic imaging have revealed submegabase, fine-scale structural features within individual chromosomes, including chromatin loops (11) and topologically associating domains (12,13). These structures can facilitate interactions between regulatory elements that are far apart in the genome to control gene expression. Significant progress has also been made in underpinning the molecular mechanisms that give rise to such structures (14–18).

However, at a global level, the presence of robust features of large-scale genome organization across chromosomes is debatable (19–21). General trends do exist, and different chromosomes tend to occupy preferred nuclear locations, with active and inactive chromatin residing near the nuclear interior and periphery, respectively (22). Conservation of the relative distances from chromosomes to nuclear speckles has also been found in a recent study (23), and variations in gene-speckle distances are generally correlated with changes in gene expression levels (24–26). On the other hand, global genome organization also exhibits evident disorder. Significant fluctuations in the spatial locations of chromosomes can be readily seen in microscopic images of individual cells

---

Submitted October 5, 2022, and accepted for publication March 1, 2023.

*Correspondence: binz@mit.edu

Editor: Helmut Schiessel.

https://doi.org/10.1016/j.bpj.2023.03.003

(27–30). Chromosome radial positions are not strictly inherited across cell cycles either (31), arguing against a significant functional role that might justify their maintenance.

A coherent mechanism that reconciles the various observations of global genome organization is currently missing. Phase separation has been proposed to drive the genome-wide compartmentalization of euchromatin and heterochromatin (32–35). However, a block copolymer model with attractive interactions between compartments of similar types fails to position heterochromatin toward nuclear envelope (36,37). In addition, chromosome-only models neglect contributions from nuclear bodies, which are increasingly appreciated for their impact on genome structure and dynamics. Several recent experimental techniques, including DNA adenine methyltransferase identification (DamID) (38), split-pool recognition of interactions by tag extension (SPRITE) (39), and tyramide signal amplification sequencing (TSA-seq) (40), have revealed close contacts between chromosomes and lamina, nucleoli, and speckles. These contacts are mediated by specific proteins and RNA molecules (25,26,41) and could significantly impact the nuclear localization of chromatin and the radial positioning of chromosomes. They needed to be explicitly accounted for a complete mechanistic understanding of genome organization (42–48).

Here, we use a data-driven mechanistic modeling approach to elucidate the mechanisms of global human genome organization. In addition to accounting for the polymeric nature of individual chromosomes, we include particle-based representations for nucleoli, speckles, and nuclear lamina. Interactions within and among various components of the nucleus describe a coupled phase separation model for the diploid genome and nuclear bodies, which we term cophase separation. After parameterization with Hi-C data, the nucleus model enables molecular dynamics simulations of genome structure and dynamics. Simulated 3D structures reproduce large-scale features of Hi-C data, correlate strongly with lamin-B1 DamID and SON TSA-seq, and match well with single-cell multiplexed genome imaging data. The cophase separation model further captures the heterogeneous organization while producing well-defined distances between speckles and euchromatin. Speckles form through nucleation on chromatin segments, giving rise to close contacts that are preserved for a long time due to slow chromosome dynamics; given the nonspecificity of phase separation, different sets of chromatin segments may nucleate speckle formation in different cells. Such heterogeneous contacts could further drive variations in chromosome positions. Together, our study highlights the significant impact of nuclear bodies on genome structure and dynamics.

MATERIALS AND METHODS

Detailed setup of nucleus model

We modeled all 46 chromosomes of the diploid human genome at 1 MB resolution using a total of 6106 coarse-grained beads. Each chromatin bead was assigned as compartment A, B, C, or N. A/B compartments were determined from the first eigenvectors of the intrachromosomal Hi-C contact matrices, and those in compartment C were identified as centromeric regions based on the DNA sequence. Compartment N denotes genomic regions that cannot be assigned as either A, B, or C due to a lack of Hi-C data. No interaction parameters were assigned for compartment N. In addition to the compartment assignments, each chromatin bead was provided with three probabilities ($P^{\mathrm{N}}, P^{\mathrm{S}}$, and P^{L}) that denote their tendency to interact with the three nuclear landmarks. More details on computing these probabilities are provided in the supporting material. Based on super-resolution imaging data (49), we estimated the size of each bead as 385 nm.

The energy function of the genome model is defined as

$$U_{\mathrm{Genome}}(\mathbf{r}) = U(\mathbf{r}) + U_{\mathrm{ideal}}(\mathbf{r}) + U_{\mathrm{compt}}(\mathbf{r}). \quad \text{(Equation 1)}$$

$U(\mathbf{r})$ represents a generic potential applied to each chromosome to ensure the polymeric topology of chromosomes. The ideal potential, $U_{\mathrm{ideal}}(\mathbf{r})$, is applied to genomic loci within the same chromosome to account for nonspecific intrachromosomal potentials that approximate the effect of loop extrusion-mediated folding and others. The contact function in this potential is parameterized from DNA-MERFISH (Multiplexed Error-Robust Fluorescence in situ Hybridization) imaging data (see supporting material and Fig. S23). $U_{\mathrm{compt}}(\mathbf{r})$ accounts for compartment-specific interaction potential that may arise from phase separation and take effect both within and across chromosomes. Detailed mathematical expressions for the potential are provided in the supporting material.

The number of coarse-grained particles for nucleoli (300) and speckles (600) was estimated based on the experimentally reported values of nuclear protein NPM1 concentration as done in a recent study (50) and the protein densities calculated from refractive index measurements (51). The size of these particles was estimated as 192.5 nm based on the average radius of individual nucleoli and speckles. We note that the above estimation is crude. The nucleolar and speckle particles should be viewed as molecular aggregates rather than a single protein molecule. Given the size of a typical protein is 5–10 nm (52), the number of molecules within a single coarse-grained particle can be on the order of 10^3. This number, while large, is on the same order as the number of distinct molecules that make up the nucleoli (53).

We used the Lennard-Jones (LJ) potential to approximate interactions between the nucleolus particles and reproduce the desired size and number of nucleoli. The potential for a particle i and j with a distance of r_{ij} adopts the form

$$U_{\mathrm{LJ}}(r_{ij}) = 4\epsilon\left(\left(\frac{\sigma}{r_{ij}}\right)^{12} - \left(\frac{\sigma}{r_{ij}}\right)^{6}\right) - U_{\mathrm{cut}} \quad \text{(Equation 2)}$$

for $r_{ij} \le r_c$ and 0 otherwise. U_{cut} is the standard shift of the LJ potential, which ensures that the potential energy function is 0 at the cutoff r_c. We used a $\epsilon = 2$ with $r_c = 2$. The size of nucleolar particles σ was set as 0.5 as estimated in the supporting material section nucleoli and speckles as phase-separated droplets. The simulation results are rather insensitive to the parameter choices, as shown in a previous study (37).

We observed that a simple LJ potential (as done for the nucleoli) could not yield a large number of speckles (see Fig. S3). In a model with LJ interactions for speckle-speckle and chromatin-speckle, we observed that small speckle clusters eventually fuse to form larger clusters, thereby reducing the total number of clusters in the system. Accordingly, we hypothesized that the many small speckle clusters are stable because of two different fundamental forces: 1) short-range attraction between speckle particles and 2) long-range repulsive forces between speckle clusters. The repulsive forces could arise from electrostatic interactions between RNA and protein molecules. Additionally, the repulsion could serve as an effective strategy for capturing the impact of chemical reactions on phase separation. In particular, phosphorylation could suppress the multivalent interactions that drive phase separation and arrest the growth of liquid droplets.

Thus, the speckle-speckle interaction we use is a linear super-position of the LJ and the Yukawa potential (54) given by

$$U(r) = U_{\mathrm{LJ}}(r) + \left(A\frac{e^{-\kappa r}}{r} - U_{\mathrm{cut}}^{\mathrm{Yuk}} \right), \qquad \text{(Equation 3)}$$

where $U_{\mathrm{LJ}}(r)$ is the potential defined in Eq. 2. We set the LJ parameters as $\epsilon = 8$ and $\sigma = 0.5$. The parameters associated with the Yukawa portion of the potential are $\chi = 0.95$, $\kappa = 1/\chi$, and $A = 2.5\chi$. The Yukawa term is a long-range repulsive term, and accordingly, the cutoff used is 6.0χ, unlike the $r_c = 2$ for the LJ portion. $U_{\mathrm{cut}}^{\mathrm{Yuk}}$ is again a shift term that ensures that the potential energy function is 0 at the cutoff r_c.

No specific interactions were included for lamina-lamina particle interactions since they were fixed during simulations. The lamina particles contain the nucleoli and speckles inside the nucleus through a short-range truncated and shifted LJ potential (Eq. 2) with $\epsilon = 1, \sigma = 1$, and $r_c = 1.12$. The interaction of the lamina with the chromatin is discussed in detail in the next section.

The three nuclear landmarks incorporated in this work are lamina, nucleoli, and speckles. Interactions between chromatin and the nuclear landmarks were described by the LJ potential defined in Eq. 2. The epsilon in these interactions is chromatin bead and landmark specific, and a detailed discussion on these values is provided in the supporting material. The base values are 0.75, 1.5, and 1.5 for lamina, nucleolus, and speckle interactions respectively. These base values are then rescaled by SPIN (Spatial Position Inference of the Nuclear genome) state probabilities.

Molecular dynamics simulation details

We used the software package LAMMPS (55) to perform molecular dynamics simulations in reduced units. Constant-temperature ($T = 1$ in reduced unit) simulations were carried out via the Langevin dynamics with a damping coefficient $\gamma = 10$ and a simulation time step of $dt = 0.005$. We froze the lamina particles and only propagated the dynamics of chromatin, nucleoli, and speckles. Configurations were recorded every 2000 simulation steps for analysis. The initial configurations of independent molecular dynamics simulations were built as follows. We first obtained whole-genome structures by uniform sampling from a 20-million-step-long trajectory carried out in our previous study (37). This trajectory was obtained without constraints of nuclear bodies and captures the large fluctuation of chromosome positions. Next, 300 nucleoli and 600 speckle particles were placed with random positions inside the nucleus. We ran a short minimization to remove any potential overlaps before carrying out each simulation for a total of 12 million time steps. The first six million time steps of each trajectory were discarded as equilibration.

Data processing and analysis

Experimental data

We obtained the in situ Hi-C data of human foreskin fibroblast (HFF) cell lines from the 4DN data portal. Hi-C experiments probe the contact frequency between pairs of genomic segments inside the nucleus using formaldehyde mediated cross-linking. The intra- and interchromosomal interactions were calculated at 1 MB resolution with VC_SQRT normalization applied to the interaction matrices. Hi-C data extraction and normalization were performed using Juicer tools (56). For Hi-C subcompartments, due to the lack of annotations for HFF cells, we used the corresponding results for IMR90 cells produced by SNIPER (Subcompartment iNference using Imputed Probabilistic ExpRessions) (57) for data analysis. Since both are fibroblast cells, we anticipate strong similarity in their subcompartment annotations. SON TSA-seq data in HFF cell line is obtained from the 4DN data portal. The TSA-seq processing and normalization method is described in (23). The protein SON is a highly specific marker for nuclear speckles. Therefore, labeling DNA with free radicals concentrated around SON and produced via TSA provide estimations of mean chromosomal distances from nuclear speckles genome-wide (23,40). Lamin-B DamID data in the HFF cell line are obtained from the 4DN data portal. Two biological replicates were merged, and the normalized counts over Dam-only control were used for analysis. DamID detects the binding sites of specific proteins by marking the corresponding DNA segments with adenine methylation. When the methyltransferase is fused with lamin-B, a scaffolding component of the nuclear envelope, the technique identifies chromosome regions contacting lamina.

The SON TSA-seq and lamin-B DamID data were processed at 25 kB resolution, and the average values at the 1 MB resolution were used in Fig. 3 for model validation. As the subcompartment annotation was performed at the 100 kb resolution, we assigned each 1MB bead in our model with probabilities for being in various subcompartments estimated from arithmetic means. We further assigned beads as $A1$ when computing Fig. 6 if the corresponding probabilities were higher than 0.5.

Simulation data

Complete details on the analysis of simulated structures can be found in the supporting material, and here we briefly describe the procedure. To compare with SON TSA-seq data, we used the DBSCAN (Density-Based Spatial Clustering of Applications with Noise) algorithm (58) to identify speckle clusters in our simulations and, consecutively, the distances of the speckles from different chromatin segments. We calculated the in silico SON TSA-seq signal for a chromatin segment using a speckle distance-dependent contact function. The signals were then converted into enrichment scores after calculating the genome-wide averages of TSA-seq signals.

For the comparison with lamin-B DamID, we used the radial positions of chromatin segments to calculate the distance from the lamina, which is an input to a contact function. We calculated the in silico DamID signals as the contact probabilities across all simulation trajectories.

RESULTS

A cophase separation model for the genome and nuclear bodies

Polymer simulations are useful tools for the mechanistic exploration of genome organization (59–62). They have been crucial for revealing the role of phase separation and loop extrusion in nuclear organization (14,15,32,34,35,44,63–72). In particular, the data-driven mechanistic modeling approach introduced in (37) directly links the quality of simulated genome structures with an energy function designed based on specific mechanisms of genome organization. As Hi-C data can constrain parameters of the energy function, the model's performance in reproducing experimental data will be mainly determined by the quality of mechanistic assumptions rather than the uncertainty of parameters. Such a strategy is valuable for screening hypotheses and identifying mechanisms of global genome organization.

We generalize the data-driven mechanistic modeling approach to simulate the human nucleus. Each of the 46 chromosomes was represented as a beads-on-a-string polymer, with each bead corresponding to a 1-MB-long genomic segment (see Fig. 1). We labeled each chromatin bead as compartment A, B, or C for euchromatin, heterochromatin, or pericentromeric regions. Compartment-type-specific interactions were incorporated to promote their phase separation. In addition to the block copolymer setup, we introduced intrachromosome interactions that vary as a function of the

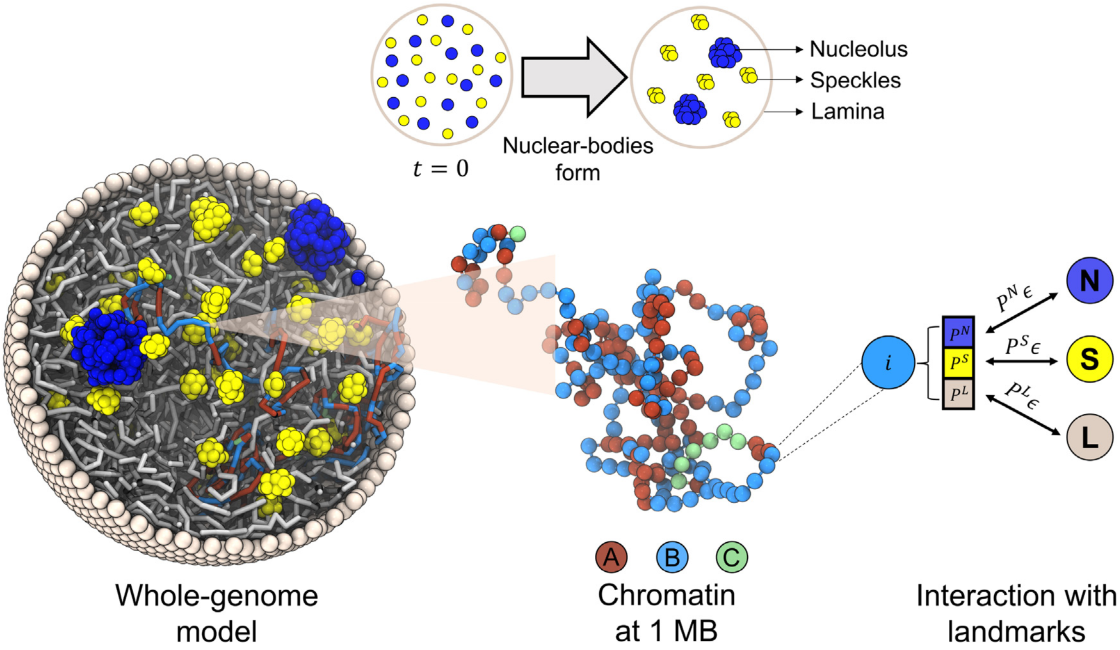

FIGURE 1 Illustration of the whole-genome model that explicitly considers chromosomes and various nuclear landmarks, including lamina (*gray*), nucleoli (*blue*), and speckles (*yellow*). Chromosomes are modeled as beads-on-a-string polymers at 1 MB resolution where the beads are further classified into euchromatin (*red*, compartment *A*), heterochromatin (*light blue*, compartment *B*), and centromeric regions (*green*, compartment *C*). As shown by the schematic in the top panel, nucleoli and speckles form through the self-assembly of coarse-grained particles uniformly distributed inside the nucleus at the beginning of simulations. Coupling between chromosomes and nuclear landmarks is accounted for with specific interactions, the strength of which depends on the contact probabilities (P^N, P^S, and P^L) between them quantified using high-throughput sequencing data (see text). To see this figure in color, go online.

sequence separation between two genomic segments. This "ideal" potential accounts for the role of specific protein molecules, such as loop extrusion via cohesin molecules (14,15), and drives chromosome territory formation (33,73). Interactions among chromatin beads were optimized to reproduce various average contact probabilities determined from Hi-C experiments for HFF cells using the maximum-entropy optimization algorithm (74–76).

In addition to the diploid genome, we adopted particle-based representation for various nuclear landmarks. We approximated the lamina as a spherical enclosure with a 10 μm diameter using discrete particles placed on a Fibonacci grid. The dynamics of the nuclear envelope was not considered, and the particles were fixed during simulations. Both nucleoli and speckles were modeled as liquid droplets (77,78) that form through spontaneous phase separation of coarse-grained particles. These particles represent protein and RNA molecule aggregates and share attractive interactions within the same type to promote condensation.

Coupling between chromatin and nuclear landmarks was accounted for with weak attractive interactions. Since their contacts are mediated by specific protein and RNA molecules (25,26,41), not all chromatins will form favorable contacts with every nuclear landmark. To ensure specificity, we further rescaled the strength of these interactions depending on the intrinsic state of chromatin beads. Three states, including speckle, nucleolus, and lamina states, corresponding to the respective nuclear landmarks, were defined using SPIN (79). SPIN annotates chromatins based on their relative position with respect to various nuclear structures through an integrative analysis of TSA-seq and DamID with Hi-C data (79). We combined the 25-kb-resolution SPIN annotations to assign each chromatin bead three probabilities for being in each state. These probabilities estimate the fraction of various states in the 1-MB-long regions and were used to renormalize chromatin-nuclear landmark interactions. They allow the model to partially account for the heterogeneity of chromatin content with a low-resolution model (Fig. S1).

We tuned the interaction parameters for nuclear particles to reproduce the corresponding nuclear bodies' number and maximize the agreement between simulated and experimental DamID and TSA-seq data (see Fig. S2). Attractive interactions between nucleolar particles and chromatin (see below) are sufficient to produce 2–3 nucleoli (50). The chromatin network can nucleate phase separation and arrest the system in multidroplet states. However, a similar treatment for speckles failed to produce experimental numbers on the order of 30–40 (see Fig. S3). Instead, we introduced repulsive interactions in the form of the Yukawa potential in addition to attractive interactions among speckle particles. The Yukawa potential has been widely used for modeling colloids and is known to stabilize the multidroplet state (80). It can serve as an effective approximation to account for the impact of nonequilibrium modification to protein molecules that disrupts droplet coarsening (81,82). We further explored a kinetic scheme of speckle formation that explicitly accounts for the chemical modification of protein molecules (83). As shown in Fig. S4, such a nonequilibrium model produces nuclear organizations that are comparable to those obtained from simulations with the Yukawa potential. Therefore, the Yukawa potential represents an accurate and computationally efficient strategy for modeling speckles and was used to generate all results presented in the main text. Detailed expression of the energy function and parameter values can be found in the supporting material.

Validating model against sequencing data

Our computational model was designed with the assumption that the genome and nuclear bodies form through self-assembly during the early G1 phase. In particular, the euchromatin and heterochromatin phases separate with the presence of nucleolar and speckle particles that themselves organize into liquid droplets. However, the validity of our assumption depends on whether the cophase separation model between chromosomes and nuclear bodies can produce structures that capture various features of nuclear organization. Upon parameterizing the interaction potentials, we extensively validated the simulated chromosome structures and chromosome-nuclear landmark contacts against experimental data to evaluate our model.

We carried out molecular dynamics simulations of the self-assembly process, which organizes genome structures and drives the formation of nuclear bodies. A total of 100 independent, 12-million-time-step-long trajectories were simulated to yield an ensemble of 3D structures. The trajectories were initialized with chromosome configurations obtained from a separate sampling of a genome model introduced in a previous study (37), though simulations starting from randomly distributed chromosome configurations produced similar results (Fig. S5). Nucleolar and speckle particles were randomly distributed throughout the nucleus. The initial period of the simulations (six million time steps) corresponds to a maturation process during which nucleoli and speckles form through spontaneous phase separation. While the dynamics of the maturation process is of interest, we did not include them for structural analysis.

We first examined the contacts between simulated chromosome structures and compared those with Hi-C experiments. As shown in Fig. 2, the chromosomes form territories and occupy spatially distinct regions (22). A/B compartments phase separate from each other, with B compartments preferentially localizing toward the nuclear periphery. The compartmentalization is evident both at the genome-wide scale and for individual chromosomes (see Fig. 2 *c*). Genome compartmentalization can also be seen from the checkerboard pattern of the simulated contact map (Fig. 3 *a*), which

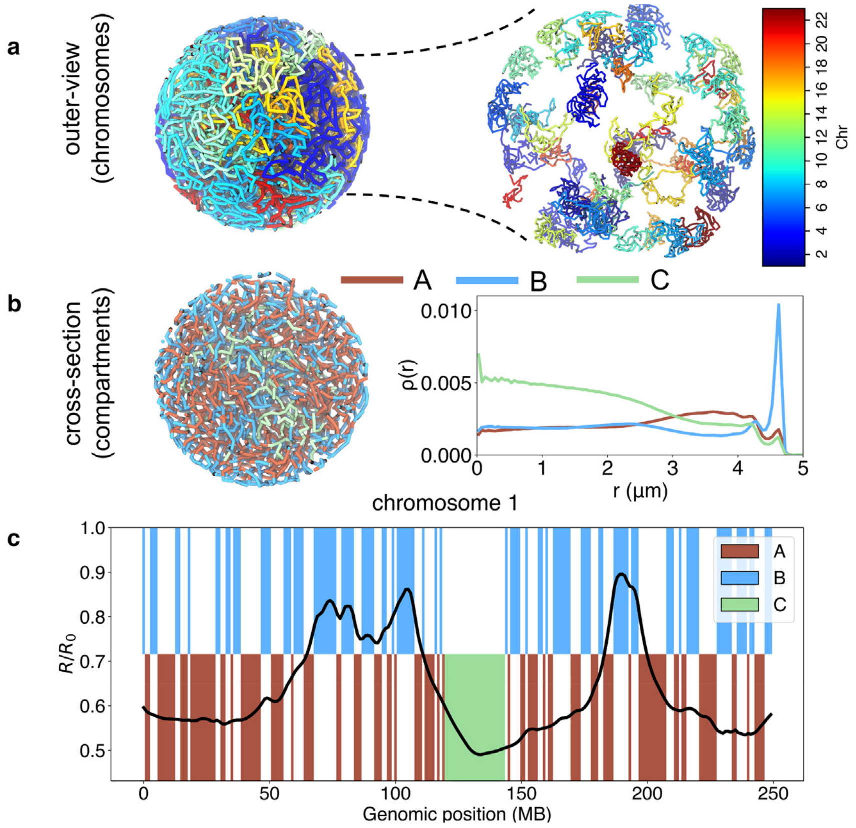

FIGURE 2 Model yields structures commensurate with chromosome territory formation and phase separation between euchromatin and heterochromatin. (*a*) Outer view of the genome colored by chromosomes (homologs have the same color) and a blown-up version. (*b*) A cross-section of the nucleus is shown with chromatin colored by the compartment type, with A in red, B in blue, and C in green. The radial density of profiles of the three compartment types are shown on the side. (*c*) The average radial position of chromosome 1 as a function of the genomic position with comparison to the compartment profile. Here, R_0 is the radius of the nucleus, and $R_0 = 13\sigma = 5$ μm. To see this figure in color, go online.

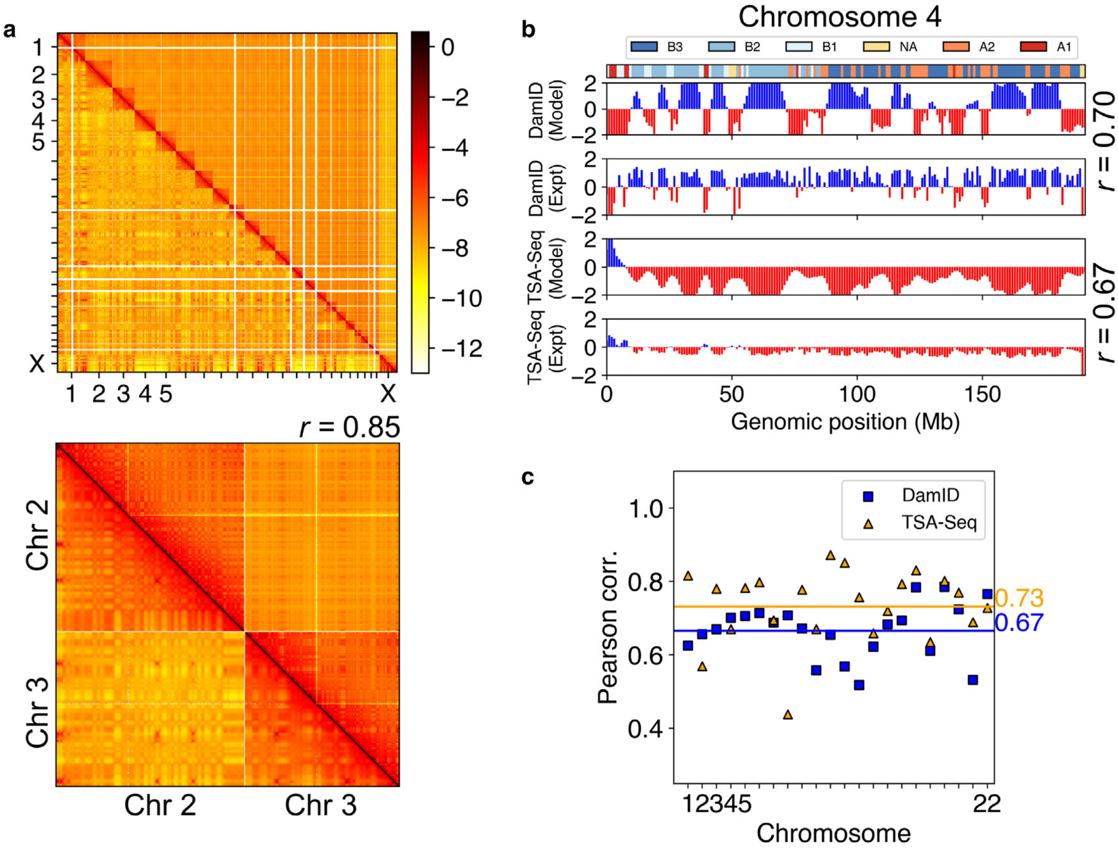

FIGURE 3 Simulated structures reproduce contacts within DNA segments and interactions between chromosomes and nuclear bodies. (*a*) Comparison between simulated (*bottom triangle*) and experimental (*top triangle*) contact matrix (84). A zoomed-in contact map between chromosomes 2 and 3 is shown with the Pearson's correlation coefficient (*r*). (*b*) Comparison (for chromosome 4) between the model predicted lamin-B DamID and SON TSA-seq signals and the experimental data at 1 MB resolution, with the Pearson's correlation coefficients shown on the side. The subcompartment annotations at the top of the figure were taken from the IMR90 cell type (fibroblast) (57). (*c*) Pearson correlation coefficients between simulated and experimental lamin-B DamID (*blue*) and SON TSA-seq (*yellow*) data for individual chromosomes. The genome-wide averages are shown as straight lines with the corresponding values on the side. To see this figure in color, go online.

matches well with Hi-C data (see also Fig. S6). These maps support high contact frequencies within the same compartment and a depletion of contacts across compartments. Additionally, we computed the average contact probability between pairs of chromosomes. The reasonable agreement between simulated and experimental values suggests that phase separation and contacts with nuclear bodies contribute to interchromosome interactions (Fig. S6 *c*). The remaining discrepancy potentially arises from chromosome-specific interactions that the model does not capture.

We computed chromatin-speckle and chromatin-lamina contacts to yield in silico predictions of the SON TSA-seq and lamin-B DamID signals, respectively. The simulated and the experimental SON TSA-seq signals (23) are in good agreement with a consistent trend, as shown in the bottom two panels of Fig. 3 *b* for chromosome 4. The Pearson correlation coefficient between the two is 0.67 (chromosome 4), and the genome-wide average correlation score is 0.73 (Fig. 3 *c*). The DamID signals are also reproduced satisfactorily, with a genome-wide correlation score of 0.67. We note that the 1 MB resolution used in our model may be insufficient to capture the sharp transitions between contact-enriched (shown in *blue* in Fig. 3 *b*) and contact-depleted zones (shown in *red*) with short periods, preventing a perfect reproduction of experimental data. Further increasing the model resolution to 100 kB indeed produced more refined genome structures that better capture the heterogeneity within chromatin domains (Fig. S7), though at greater computational expense. As shown in the following sections, the 1 MB model's computational efficiency allows comprehensive mechanistic exploration of the coupling between chromatin organization and nuclear landmarks.

Validating model against imaging data

In addition to sequencing-based genomic mapping data, we utilized the multiplexed 3D genome imaging data to further evaluate our model. Recent advancements in microscopy imaging-based techniques have enabled simultaneous detection of hundreds to thousands of distinct genomic loci (28,85). These imaging data provide valuable information on the 3D positions of genomic regions at single-cell resolution for more direct comparisons with the simulated structures in order to benchmark the quality of our model.

We first examined that in our simulations, the nuclear bodies formed through self-assembly of individual particles that are randomly distributed at the start. As shown in Fig. S8, the average number of nucleoli (2) and speckles (36) are in good agreement with values estimated from microscopic images (86,87). While the classical nucleation theory would predict an equilibrium state with single droplets, the attractive interactions between nucleoli and chromatin help arrest droplet coalescence, stabilizing the multidroplet state (50). The weak but long-ranged repulsive interactions in addition to the short-ranged attractive interaction among the speckle particles further suppress droplet coarsening, producing an order of magnitude more speckles than nucleoli.

We further evaluated chromosome conformations against imaging data. As shown in Fig. 4 *c*, the simulated radial chromosome positions are highly correlated with experimental values (27) with a Pearson correlation coefficient of 0.68. The radius of gyration of individual chromosomes matches well with DNA-MERFISH imaging data (see Fig. 4, *a* and *b*) that report the spatial positions of uniformly selected loci across chromosomes in individual cells (28).

Finally, we characterized the localization of specific genomic regions relative to nuclear bodies. In previous studies, chromatin compartments are further classified into subcompartments that have distinct features (11,89–91). One of the most commonly used classifications is to sort the genomic loci based on long-range interaction patterns dividing the A and B compartments in $A1$, $A2$, $B1$, $B2$, and $B3$. $A1$ and $A2$ are known to be gene-dense segments and rich in the histone marks H3K36me3, H3K79me2, H3K27ac, and H3K4me1 (11). On the contrary, $B1$, $B2$, and $B3$ are representative of heterochromatin and are gene-lean segments that are typically enriched toward the nuclear lamina. Subcompartments provide a more nuanced classification of chromatin than compartments A/B to distinguish the varying degrees of gene activation/repression and contacts with nuclear landmarks (40).

We found that the simulated contacts are in qualitative agreement with DNA-MERFISH imaging results (Fig. 4 *d*).

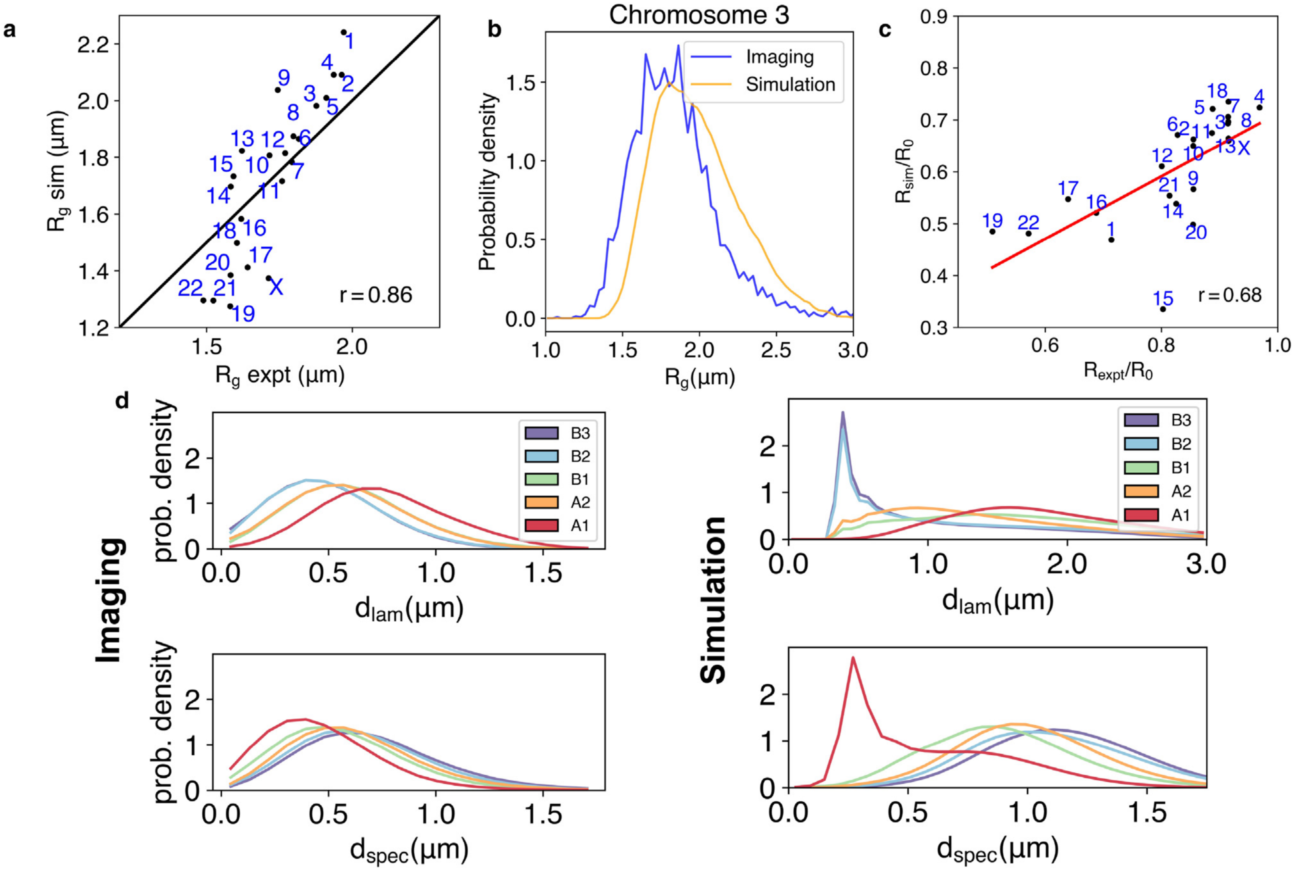

FIGURE 4 Simulated structures reproduce chromosome sizes, positions, and the localization of genome subcompartments. (*a*) Comparison between chromosome radius of gyrations from simulations and from DNA-MERFISH experiments (28). The Pearson's correlation coefficient ($r = 0.86$) is also shown. (*b*) Overlap of the probability distributions for the radius of gyration of chromosome 3 computed from the experimental and simulated structural ensemble. (*c*) Comparison of the chromosome radial positions in experiment (88) and simulations. Here, R_0 is the radius of the nucleus, and $R_0 = 13\sigma = 5\ \mu\text{m}$. (*d*) Distribution of genome subcompartments as a function of distance from nuclear lamina (d_{lam}) and speckles (d_{spec}), respectively, shown for DNA-MERFISH imaging (28) and simulation data. To see this figure in color, go online.

For example, subcompartments $A1$ and $B3$ strongly localize in close proximity to speckles and nuclear lamina, respectively. Additionally, subcompartments $A2$ and $B2$ occupy intermediate regions transitioning between speckles and nuclear lamina. $A2$ is localized more toward speckles, while $B2$ is close to the nuclear lamina. We note that a quantitative comparison with imaging data was not attempted because we used a spherical model for the nuclear lamina, while cells in experiments are more ellipsoidal (see Fig. S9). Analyses on the spatial distribution of two types of lamina-associated domains: constitutive and facultative revealed good agreement between simulation and single-cell imaging data as well (Fig. S10).

It is worth pointing out that our model only recognizes A and B compartments but was not explicitly provided with the subcompartment annotations. Its success in differentiating the spatial localization of subcompartments arises from the chromatin-nuclear landmark interactions specified by the three different states. For example, $A1$ and $B3$ strongly correlate with speckle and lamina states (79), resulting in their preferential contacts with the respective nuclear landmarks seen in Fig. 4. Together, the specificity incorporated by the three states and compartment types provides complementary representations of the genome to capture the distinct aspects of nuclear organization.

Interactions with speckles refine A compartments

Our extensive validations support the cophase separation model for chromosome organization and nuclear body formation. The coupling between chromatin and nuclear lamina helps position heterochromatin toward the nuclear periphery (68,92). Without such coupling, we previously showed that heterochromatin would occupy interior locations (37). The impact of speckles on euchromatin is less clear since the phase separation between euchromatin and heterochromatin will naturally place them toward nuclear interior. Whether speckles reinforce euchromatin's interior position remains to be seen.

To probe the impact of speckles on genome organization, we perturbed the system to induce speckle coalescence by weakening the repulsive potential between speckle particles (Fig. 5 *a*). Fusing droplets could bring associated chromatin segments together, exerting a pulling force on the genome, as shown by Brangwynne and co-workers (93). We found that the spatial distribution of A compartments was altered significantly as speckle numbers decreased from 40 to 10. Speckles and euchromatin tend to shift toward the nuclear interior to maximize contacts with A compartments coming from all directions upon coalescence. A similar movement of speckles has indeed been seen in cells with inhibited transcription that induce speckle fusion (94). We further broke down the impact into two subcompartments (see Fig. 5 *b*). As expected, there is a significant perturbation to $A1$ subcompartments that directly interact with speckles. We found the distribution of $A2$ is altered as well, though to a lesser extent. Since most $A2$ subcompartments do not directly contact speckles, their impact is an indirect effect mediated via $A1$ as a result of the attraction among all A compartments.

The coupling between speckle fusion and chromatin interior movement shown in Fig. 5 arises from the overlap between the speckle state and the subcompartment $A1$ (40,79). Given the correlation, it is tempting to hypothesize that the partition of compartment A into two subcompartments results from their differential contacts with nuclear speckles. This hypothesis implies that interacting with speckles alters the contact patterns between the subset of A compartments with the rest of the genome. As a test of this hypothesis, we performed a Gaussian hidden Markov model clustering of all A compartment beads based on their interchromosomal contact patterns. The same procedure introduced in Rao et al. (11) that led to the annotation of subcompartments was adopted here. As shown in Figs. 5 *c* and S11, the two clusters identified from our simulated contact map indeed correlate well with $A1/A2$ annotations based on the Hi-C data. Therefore, differential contacts with speckles may underly the unique contact patterns seen in Hi-C data and the rise of subcompartments. Our results support that nuclear bodies and self-organization play an essential role in refining the compartments.

Single-cell heterogeneity and robustness

The results presented so far support that the model captures the average contacts within chromatin and between chromatin and nuclear landmarks. Next, we analyze the simulated structural ensemble to characterize the heterogeneity and fluctuation of these contacts. Specifically, we sought to ask whether the model can reconcile the apparent heterogeneity of genome organization across cells with the emergence of well-defined distances, which may appear paradoxical as discussed in the introduction.

To quantify the heterogeneity of genome organization, we computed the variance of chromosome positions and chromosome radii of gyration across a total of 100 trajectories that are initialized from distinct configurations (see materials and methods). As shown in Fig. S12, chromosome position distributions from independent simulations differ significantly, with a distribution width of about 1.4 μm. Chromosome radii of gyration also undergo substantial changes (Figs. 4 and S13) on an order that quantitatively agrees with values from DNA-MERFISH imaging (28).

In addition to the heterogeneity at chromosome levels, we further studied local chromatin organization around speckles. We computed the average contact map for $A1$ subcompartments that are known to localize close to speckles (40). Two $A1$ segments were noted as in contact if they were bound to the same speckle. Fig. 6 shows the variance of the speckle-mediated $A1$ contact map across simulation trajectories. There is a significant fluctuation, consistent with the variation

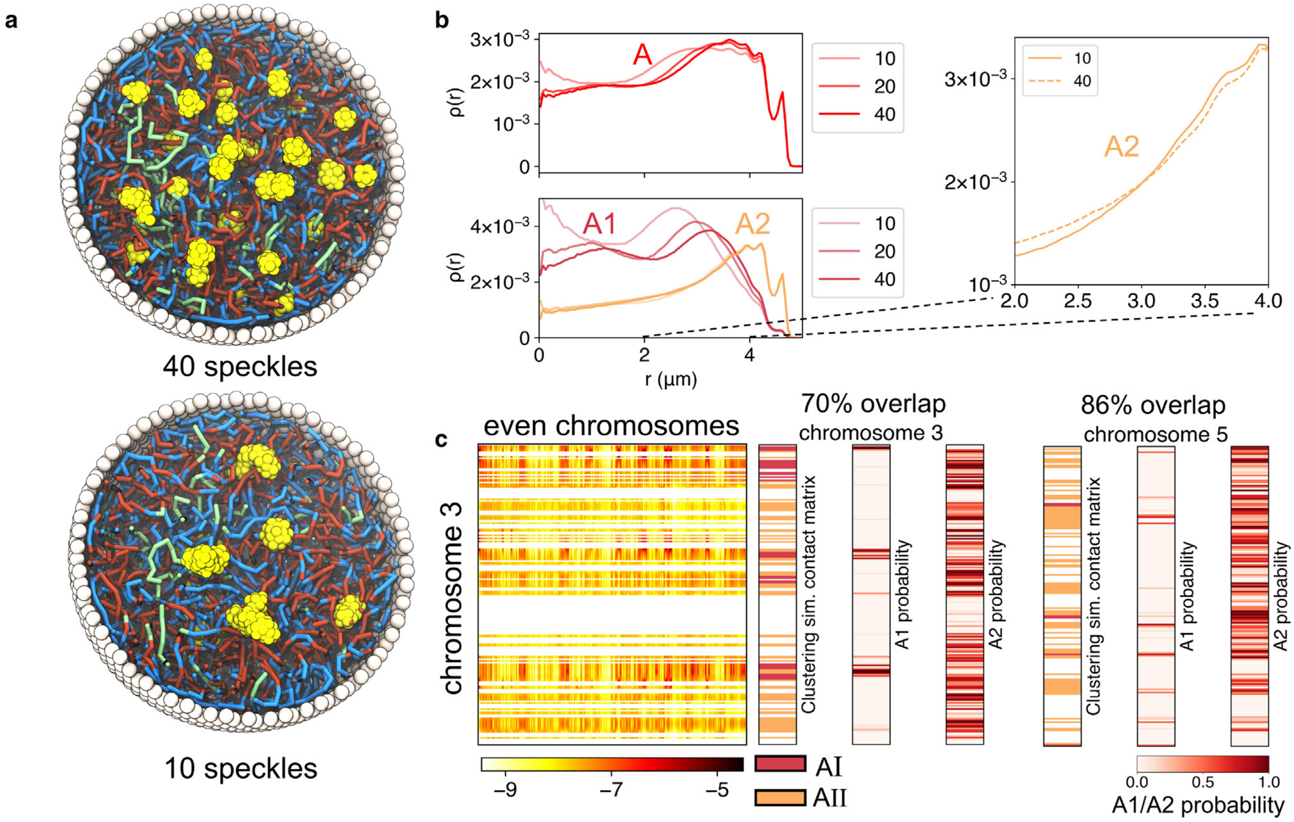

FIGURE 5 Speckles pull a subset of *A* compartments toward nuclear interior, producing their distinct contact patterns with the rest of the genome. (*a*) Cross sections of two nucleus models with 40 (*top*) and 10 (*bottom*) speckles. Speckles in the bottom panel adopt more interior localizations. (*b*) Radial densities of the *A* compartment and *A*1 and *A*2 subcompartments as a function of the radial position inside the nucleus. The top panel highlights the pulling of the *A* segments to the interior upon lowering the number of speckles in the system. The lower panel highlights the behavior of the *A*1 and *A*2 segments upon perturbing the number of speckles in the system. (*c*) Comparison between the two subtypes of *A* compartments (*AI* and *AII*) and *A*1 and *A*2 subcompartment annotation probabilities for chromosomes 3 and 5. The simulated genome-wide contact matrix between the *A* loci on chromosome 3 and all even chromosomes is shown on the left. This contact matrix was used for clustering the *A* loci into two subtypes (see also Figure S11). To see this figure in color, go online.

of chromosome positions shown in Fig. S12. The magnitude of the contact probabilities matches well with that determined from DNA-MERFISH imaging (see Figs. S14 and S15). This variation arises from the nonspecificity of phase separation: while *A*1 segments almost always interact with the speckle particles and nucleate their condensation, different sets of *A*1 may contribute to such interactions in different trajectories. Chromatin-speckle interactions are key for giving rise to heterogeneity of genome organization. As shown in Fig. S16, upon removing these interactions, the heterogeneity among *A*1-*A*1 contacts across trajectories almost vanished, and the system can equilibrate these contacts on simulation timescales.

In contrast to the large fluctuations across independent trajectories, we found that the contacts among *A*1 evaluated at different time points of the same trajectory are relatively robust with minimal changes (see Figs. 6, *bottom panel*, and S17). Minimal variations within one trajectory arise since speckle-chromatin interactions are strong and can last for a long time. The *A*1 segments are essentially glued to their *A*1 counterparts, which were formed at the beginning of phase separation. Therefore, the cophase separation model, in which speckles nucleate around chromatin segments, captures both the random and precise nature of genome organization.

DISCUSSION

In this work, we developed a molecular simulation framework to study the human genome organization and explore mechanisms for its setup. In addition to polymer models of chromosomes, we explicitly incorporated particle-based representations of nuclear lamina, nucleoli, and speckles. The 3D organization of chromosomes and the formation of nuclear bodies were modeled as a self-assembly process driven by the various interaction energies in the system. Such self-assembly simulations reproduced global features of genome structures, the number of nuclear bodies, and the contacts between the genome and nuclear landmarks. Our results support the hypothesis that nuclear landmarks largely compartmentalize the genome by attracting active

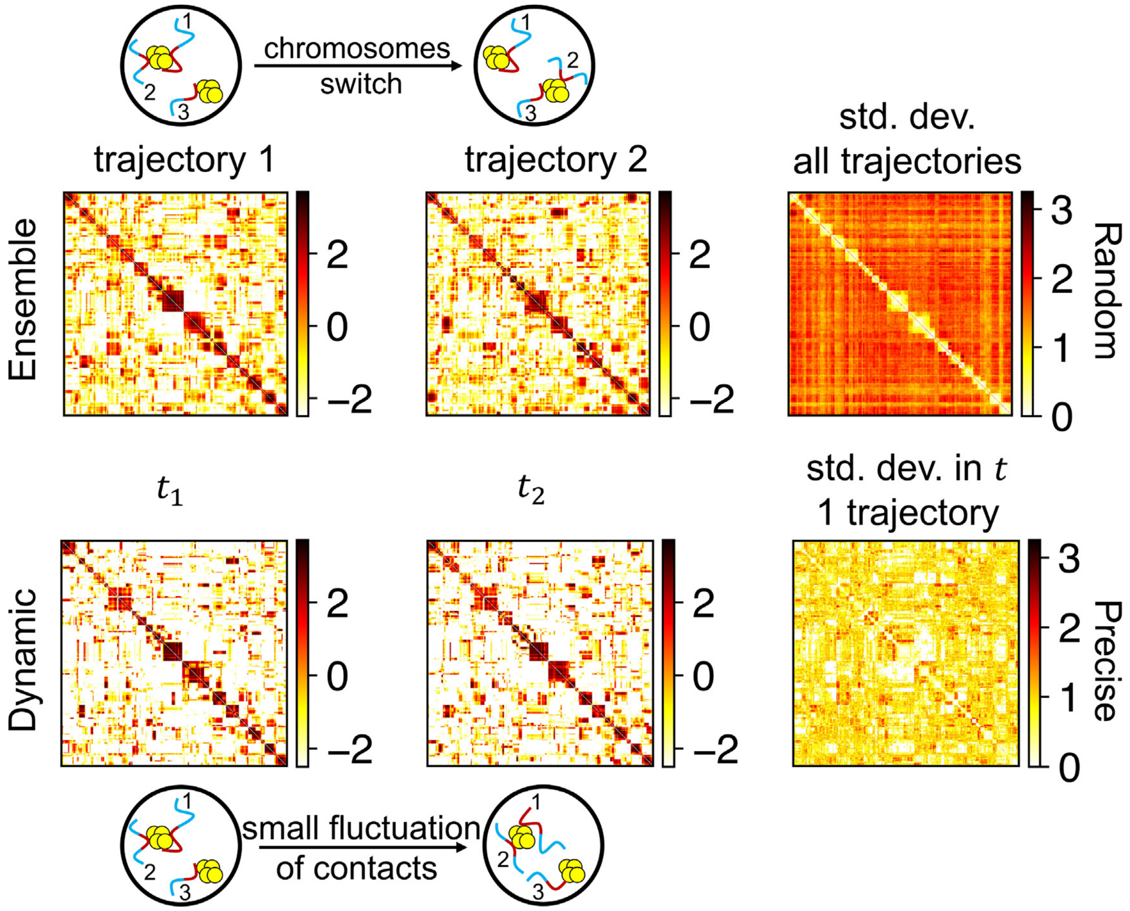

FIGURE 6 Variation of speckle-mediated contacts between genomic segments of $A1$ subcompartments. The left two matrices in the top panel show the average $A1 - A1$ contact matrix calculated over the course of the entire trajectory for two independent simulations, and the bottom panel shows the contact matrix calculated at different times within the same trajectory. The matrix on the far right in both panels denotes the standard deviation in the contact matrices. A single trajectory of six million time steps was divided into 10 blocks to obtain the standard deviation matrix shown in the bottom panel. The dissimilarity in $A1$ contacts between different trajectories has a much higher variation compared with the variance in the contacts within a trajectory. To see this figure in color, go online.

and repressive regions to the nuclear interior and periphery, respectively.

The genome may behave as a reversible network as a result of the interactions between chromatin and various nuclear landmarks. For example, speckles could introduce transient, physical cross-links to the polymeric chromatin network, especially given that biological condensates like speckles often exhibit viscoelastic properties (95). A reversible network with physical cross-links is consistent with the arrested kinetics of speckles (94,96) and with the gel-like behavior of chromatin (97,98). It provides an intuitive explanation for the random, yet precise, global genome organization discussed in the introduction. Nuclear bodies form through nucleation on highly transcribed chromatin segments. This nucleation mainly occurs during the early G1 phase and may provide an initial memory of speckle-chromatin contacts. Physical cross-links with speckles and tethering by nuclear lamina constrain chromosome dynamics to preserve the memory, producing well-defined distances between genome and nuclear bodies. Perturbing chromatin-nuclear landmark interactions significantly altered the complex modulus of chromatin and the relaxation timescales (Fig. S18). Slow chromatin dynamics is indeed well documented in the literature (97–100), potentially as a result of interactions with nuclear bodies (101). On the other hand, because of the nonspecificity of phase separation, different sets of chromatin segments could participate in different cells to nucleate speckle formation. This heterogeneity of contacts across cells could further drive the fluctuation of chromosome radial positions. While heterogeneous, the cophase separation model does ensure that genomic regions that are highly transcribed will always reside in spatial proximity with speckles. Notably, the formation of well-defined, functionally important distances does not require thermodynamic equilibration of the system, which can be challenging given the genome's large size and the presence of nonequilibrium processes in the nucleus. Further exploring genome dynamics with the model introduced here, especially when coupled with active processes such as transcription (102–105) and loop extrusion (14,18), will present exciting future directions.

The model is interpretable by design, and individual terms of the energy function represent known mechanisms of genome organization. Neglecting any components will jeopardize the model's capacity in simulating nuclear structures. For example, we found that abolishing chromatin-lamina interactions led to a poor agreement between simulated and experimental DamID profiles (Fig. S19). Additionally, the simulated genomes structures are more dynamic (Fig. S20) and fail to reproduce experimental radial positions of chromosomes (Fig. S19 *c*). Our simulation results are consistent with several recent experimental studies that observed significant lamina-associated domain dissociation from the nuclear envelope in cells deficient in lamin proteins (106–108).

We performed simulations with removed interactions between chromatin and speckles/nucleoli as well. Not surprising, the resulting genome structures fail to produce TSA-seq profiles that match experimental values (see Fig. S21, *a* and *b*). However, this perturbation does not significantly alter chromatin-lamina interactions. Together with results shown in Fig. S19, *b* and *c*, these simulations support a decoupling between two nuclear landmarks, lamina and speckles. Their interactions with chromatin are relatively independent from one another. Surprisingly, removing chromatin-speckle interactions does not impact the radial positions of chromosomes (see Fig. S21 *c*). The agreement between simulated and experimental chromosome positions is preserved even when we further removed the compartmentalization force, i.e., by setting α_{compt} defined in Equation S9 (see Table S3 and Fig. S22) to zero. Therefore, chromatin-lamina interactions largely dictate the radial positions of individual chromosomes.

We note that in addition to the nuclear landmarks considered here, other molecules, including lamin A (109) and HP1 (110), have also been suggested to cross-link chromatin. The coarsened resolution of our model would not be sufficient to capture the impact of these molecules, which may work together with speckles to constrain the genome structure and dynamics further.

Several studies have recently attempted to reconstruct whole-genome organizations from experimental data (36,111,112). Our study is complementary to the integrative modeling approach by Boninsegna et al. (111), which combined Hi-C, lamin-B1 DamID, 3D FISH imaging, and SPRITE data to produce an ensemble of genome structures. The modeled structures were shown to predict orthogonal experimental data from SON TSA-seq and DNA-MERFISH imaging well. Like the study of Boninsegna et al. (111), our approach succeeded in building consensus structures that agree with a collection of experimental data. However, the explicit modeling of nuclear landmarks and their dynamical coupling with chromatin that are unique to this study render our approach useful for uncovering mechanisms that lead to the establishment of such structures. The model introduced by Fujishiro and Sasai (36) is more similar in spirit to our approach by designing an effective energy function of polymer models that can reproduce/explain experimental data. However, they did not consider the role of speckles in genome organization. As discussed in the main text, speckles are essential for an accurate description of the structure and dynamics of active chromatin.

Data availability

4DN: 4DNES2R6PUEK, 4DNESXZ4FW4T, 4DNEX6-U8TS3Y, 4DNEXI7XUWFK for Hi-C, LaminB DamID, SON TSA-Seq pulldown data and SON TSA-Seq control data respectively. Hi-C subcompartments data: https://cmu.app.box.com/s/n4jh3utmitzl88264s8bzsfcjhqnhaa0/folder/86847603885.

SUPPORTING MATERIAL

Supporting material can be found online at https://doi.org/10.1016/j.bpj.2023.03.003.

AUTHOR CONTRIBUTIONS

Conceptualization, K.K. and B.Z.; methodology, K.K., Z.L., Y.Q., and B.Z.; investigation, K.K., Z.L., Y.Q., Y.W., J.M., and B.Z.; visualization, K.K. and B.Z.; supervision, B.Z.; writing – original draft, K.K. and B.Z.; writing, review & editing, K.K., Z.L., Y.Q., Y.W., J.M., and B.Z.

ACKNOWLEDGMENTS

We thank Bas van Steensel for making the lamin-B DamID data for HFF cells available. This work was supported in part by the National Institutes of Health grant R35GM133580 (B.Z.) and National Institutes of Health Common Fund 4D Nucleome Program grant UM1HG011593 (J.M.).

DECLARATION OF INTERESTS

The authors declare no competing interests.

REFERENCES

1. Hübner, M. R., M. A. Eckersley-Maslin, and D. L. Spector. 2013. Chromatin organization and transcriptional regulation. *Curr. Opin. Genet. Dev.* 23:89–95. http://www.sciencedirect.com/science/article/pii/S0959437X12001360.
2. Bickmore, W. A. 2013. The spatial organization of the human genome. *Annu. Rev. Genomics Hum. Genet.* 14:67–84.
3. Gorkin, D. U., D. Leung, and B. Ren. 2014. The 3D genome in transcriptional regulation and pluripotency. *Cell Stem Cell.* 14:762–775.
4. Cremer, T., M. Cremer, …, C. Cremer. 2015. The 4D nucleome: evidence for a dynamic nuclear landscape based on co-aligned active and inactive nuclear compartments. *FEBS Lett.* 589:2931–2943. https://www.ncbi.nlm.nih.gov/pubmed/26028501.
5. Bonev, B., and G. Cavalli. 2016. Organization and function of the 3D genome. *Nat. Rev. Genet.* 17:661–678.

6. Dekker, J., and L. Mirny. 2016. The 3D genome as moderator of chromosomal communication. *Cell.* 164:1110–1121. http://www.ncbi.nlm.nih.gov/pubmed/26967279.
7. Hnisz, D., D. S. Day, and R. A. Young. 2016. Insulated neighborhoods: structural and functional units of mammalian gene control. *Cell.* 167:1188–1200. https://www.ncbi.nlm.nih.gov/pubmed/27863240.
8. Rowley, M. J., and V. G. Corces. 2018. Organizational principles of 3D genome architecture. *Nat. Rev. Genet.* 19:789–800. http://www.ncbi.nlm.nih.gov/pubmed/30367165.
9. Finn, E. H., and T. Misteli. 2019. Molecular basis and biological function of variability in spatial genome organization. *Science.* 365:eaaw9498.
10. Furlong, E. E. M., and M. Levine. 2018. Developmental enhancers and chromosome topology. *Science.* 361:1341–1345.
11. Rao, S. S. P., M. H. Huntley, …, E. L. Aiden. 2014. A 3D map of the human genome at kilobase resolution reveals principles of chromatin looping. *Cell.* 159:1665–1680. http://www.sciencedirect.com/science/article/pii/S0092867414014974.
12. Nora, E. P., B. R. Lajoie, …, E. Heard. 2012. Spatial partitioning of the regulatory landscape of the X-inactivation centre. *Nature.* 485:381–385. https://doi.org/10.1038/nature11049.
13. Dixon, J. R., S. Selvaraj, …, B. Ren. 2012. Topological domains in mammalian genomes identified by analysis of chromatin interactions. *Nature.* 485:376–380.
14. Sanborn, A. L., S. S. P. Rao, …, E. L. Aiden. 2015. Chromatin extrusion explains key features of loop and domain formation in wild-type and engineered genomes. *Proc. Natl. Acad. Sci. USA.* 112:E6456–E6465.
15. Fudenberg, G., M. Imakaev, …, L. A. Mirny. 2016. Formation of chromosomal domains by loop extrusion. *Cell Rep.* 15:2038. https://www.ncbi.nlm.nih.gov/pubmed/27210764.
16. Xie, W. J., Y. Qi, and B. Zhang. 2020. Characterizing chromatin folding coordinate and landscape with deep learning. *PLoS Comput. Biol.* 16:e1008262. https://dx.plos.org/10.1371/journal.pcbi.1008262.
17. Parmar, J. J., M. Woringer, and C. Zimmer. 2019. How the genome folds: the biophysics of four-dimensional chromatin organization. *Annu. Rev. Biophys.* 48:231–253.
18. Fudenberg, G., N. Abdennur, …, L. A. Mirny. 2017. Emerging evidence of chromosome folding by loop extrusion. *Cold Spring Harb. Symp. Quant. Biol.* 82:45–55. https://doi.org/10.1101/sqb.2017.82.034710.
19. Williams, R. R. E., and A. G. Fisher. 2003. Chromosomes, positions please. *Nat. Cell Biol.* 5:388–390.
20. Parada, L. A., J. J. Roix, and T. Misteli. 2003. An uncertainty principle in chromosome positioning. *Trends Cell Biol.* 13:393–396.
21. Bickmore, W. A., and J. R. Chubb. 2003. Chromosome position: now, where was I? *Curr. Biol.* 13:R357–R359.
22. Cremer, T., and C. Cremer. 2001. Chromosome territories, nuclear architecture and gene regulation in mammalian cells. *Nat. Rev. Genet.* 2:292–301. http://www.ncbi.nlm.nih.gov/pubmed/11283701.
23. Zhang, L., Y. Zhang, …, A. S. Belmont. 2020. TSA-seq reveals a largely conserved genome organization relative to nuclear speckles with small position changes tightly correlated with gene expression changes. *Genome Res.* 31:251–264.
24. Khanna, N., Y. Hu, and A. S. Belmont. 2014. HSP70 transgene directed motion to nuclear speckles facilitates heat shock activation. *Curr. Biol.* 24:1138–1144.
25. Alexander, K. A., A. Coté, …, S. L. Berger. 2021. p53 mediates target gene association with nuclear speckles for amplified RNA expression. *Mol. Cell.* 81:1666–1681.e6.
26. Quinodoz, S. A., J. W. Jachowicz, …, M. Guttman. 2021. RNA promotes the formation of spatial compartments in the nucleus. *Cell.* 184:5775–5790.e30.
27. Boyle, S., S. Gilchrist, …, W. A. Bickmore. 2001. The spatial organization of human chromosomes within the nuclei of normal and emerin-mutant cells. *Hum. Mol. Genet.* 10:211–219.
28. Su, J. H., P. Zheng, …, X. Zhuang. 2020. Genome-scale imaging of the 3D organization and transcriptional activity of chromatin. *Cell.* 182:1641–1659.e26. https://doi.org/10.1016/j.cell.2020.07.032.
29. Payne, A. C., Z. D. Chiang, …, F. Chen. 2021. In situ genome sequencing resolves DNA sequence and structure in intact biological samples. *Science.* 371:eaay3446.
30. Shi, G., and D. Thirumalai. 2019. Conformational heterogeneity in human interphase chromosome organization reconciles the FISH and Hi-C paradox. *Nat. Commun.* 10, 3894.
31. Thomson, I., S. Gilchrist, …, J. R. Chubb. 2004. The radial positioning of chromatin is not inherited through mitosis but is established de Novo in early G1. *Curr. Biol.* 14:166–172.
32. Jost, D., P. Carrivain, …, C. Vaillant. 2014. Modeling epigenome folding: formation and dynamics of topologically associated chromatin domains. *Nucleic Acids Res.* 42:9553–9561.
33. Di Pierro, M., B. Zhang, …, J. N. Onuchic. 2016. Transferable model for chromosome architecture. *Proc. Natl. Acad. Sci. USA.* 113:12168–12173. https://www.ncbi.nlm.nih.gov/pubmed/27688758.
34. Falk, M., Y. Feodorova, …, L. A. Mirny. 2019. Heterochromatin drives compartmentalization of inverted and conventional nuclei. *Nature.* 570:395–399.
35. Shi, G., L. Liu, …, D. Thirumalai. 2018. Interphase human chromosome exhibits out of equilibrium glassy dynamics. *Nat. Commun.* 9:3161.
36. Fujishiro, S., and M. Sasai. 2021. Generation of dynamic three-dimensional genome structure through phase separation of chromatin. Preprint at bioRxiv. https://www.biorxiv.org/content/early/2021/05/07/2021.05.06.443035.
37. Qi, Y., A. Reyes, …, B. Zhang. 2020. Data-driven polymer model for mechanistic exploration of diploid genome organization. *Biophys. J.* 119:1905–1916. https://linkinghub.elsevier.com/retrieve/pii/S0006349520307190.
38. Pickersgill, H., B. Kalverda, …, B. Van Steensel. 2006. Characterization of the Drosophila melanogaster genome at the nuclear lamina. *Nat. Genet.* 38:1005–1014.
39. Quinodoz, S. A., N. Ollikainen, …, M. Guttman. 2018. Higher-order inter-chromosomal hubs shape 3D genome organization in the nucleus. *Cell.* 174:744–757.e24. https://doi.org/10.1016/j.cell.2018.05.024.
40. Chen, Y., Y. Zhang, …, A. S. Belmont. 2018. Mapping 3D genome organization relative to nuclear compartments using TSA-Seq as a cytological ruler. *J. Cell Biol.* 217:4025–4048.
41. Khelifi, G., and S. M. I. Hussein. 2020. A new view of genome organization through RNA directed interactions. *Front. Cell Dev. Biol.* 8:517.
42. Bajpai, G., D. A. Pavlov, …, S. Safran. 2020. Mesoscale phase separation of chromatin in the nucleus. *Biophys. J.* 118:549a.
43. Lappala, A., C.-Y. Wang, …, K. Y. Sanbonmatsu. 2021. Four-dimensional chromosome reconstruction elucidates the spatiotemporal reorganization of the mammalian X chromosome. *Proc. Natl. Acad. Sci. USA.* 118:e2107092118.
44. Chiang, M., D. Michieletto, …, T. Chandra. 2019. Polymer modeling predicts chromosome reorganization in senescence. *Cell Rep.* 28:3212–3223.e6. https://doi.org/10.1016/j.celrep.2019.08.045.
45. Laghmach, R., M. Di Pierro, and D. A. Potoyan. 2021. The interplay of chromatin phase separation and lamina interactions in nuclear organisation. Preprint at bioRxiv. https://doi.org/10.1101/2021.03.16.435657.
46. Maji, A., J. A. Ahmed, …, M. K. Mitra. 2020. A Lamin-Associated chromatin model for chromosome organization. *Biophys. J.* 118:3041–3050.
47. Li, Q., H. Tjong, F. Alber…, 2017. The three-dimensional genome organization of Drosophila melanogaster through data integration. *Genome Biol.* 18, 145.

48. Paulsen, J., M. Sekelja, …, P. Collas. 2017. Chrom3D: three-dimensional genome modeling from Hi-C and nuclear lamin-genome contacts. *Genome Biol.* 18:21.
49. Boettiger, A. N., B. Bintu, …, X. Zhuang. 2016. Super-resolution imaging reveals distinct chromatin folding for different epigenetic states. *Nature.* 529:418–422. http://www.nature.com/nature/journal/v529/n7586/pdf/nature16496.pdf.
50. Qi, Y., and B. Zhang. 2021. Chromatin network retards droplet coalescence. Preprint at bioRxiv. https://doi.org/10.1101/2021.03.02.433564.
51. Handwerger, K. E., J. A. Cordero, and J. G. Gall. 2005. Cajal bodies, nucleoli, and speckles in the Xenopus oocyte nucleus have a low-density, sponge-like structure. *Mol. Biol. Cell.* 16:202–211.
52. Lee, H. H., H. S. Kim, …, S. W. Suh. 2007. Crystal structure of human nucleophosmin-core reveals plasticity of the pentamer–pentamer interface. *Proteins.* 69:672–678.
53. Scherl, A., Y. Couté, …, J.-J. Diaz. 2002. Functional proteomic analysis of human nucleolus. *Mol. Biol. Cell.* 13:4100–4109.
54. Yukawa, H. 1935. On the interaction of elementary particles. I. *Proc. Phys.Math. Soc. Jap.* 17:48–57, *3rd Series*.
55. Plimpton, S., and L. S. National. 1995. Fast parallel algorithms for short–range molecular dynamics. *J. Comput. Phys.* 117:1–19. http://www.sciencedirect.com/science/article/pii/S002199918571039X.
56. Durand, N. C., M. S. Shamim, …, E. L. Aiden. 2016. Juicer provides a one-click system for analyzing loop-resolution Hi-C experiments. *Cell Syst.* 3:95–98.
57. Xiong, K., and J. Ma. 2019. Revealing Hi-C subcompartments by imputing inter-chromosomal chromatin interactions. *Nat. Commun.* 10:5069–5112.
58. Ester, M., H.-P. Kriegel, …, X. Xu. 1996. A density-based algorithm for discovering clusters in large spatial databases with noise. *In* Kdd, *volume 96*, pp. 226–231.
59. Dekker, J., M. A. Marti-Renom, and L. A. Mirny. 2013. Exploring the three-dimensional organization of genomes: interpreting chromatin interaction data. *Nat. Rev. Genet.* 14:390–403.
60. Brackey, C. A., D. Marenduzzo, and N. Gilbert. 2020. Mechanistic modeling of chromatin folding to understand function. *Nat. Methods.* 17:767–775.
61. Zhou, R., and Y. Q. Gao. 2020. Polymer models for the mechanisms of chromatin 3D folding: review and perspective. *Phys. Chem. Chem. Phys.* 22:20189–20201.
62. Lin, X., Y. Qi, …, B. Zhang. 2021. Multiscale modeling of genome organization with maximum entropy optimization. *J. Chem. Phys.* 155:010901.
63. Bohn, M., and D. W. Heermann. 2010. Diffusion-driven looping provides a consistent provides a consistent framework for chromatin organization. *PLoS One.* 5:e12218. http://www.ncbi.nlm.nih.gov/pubmed/20811620.
64. Barbieri, M., M. Chotalia, …, M. Nicodemi. 2012. Complexity of chromatin folding is captured by the strings and binders switch model. *Proc. Natl. Acad. Sci. USA.* 109:16173–16178.
65. Gürsoy, G., Y. Xu, …, J. Liang. 2017. Computational construction of 3D chromatin ensembles and prediction of functional interactions of alpha-globin locus from 5C data. *Nucleic Acids Res.* 45:11547–11558.
66. Di Pierro, M., R. R. Cheng, …, J. N. Onuchic. 2017. De novo prediction of human chromosome structures: epigenetic marking patterns encode genome architecture. *Proc. Natl. Acad. Sci. USA.* 114:12126–12131.
67. Erdel, F., and K. Rippe. 2018. formation of chromatin subcompartments by phase separation. *Biophys. J.* 114:2262–2270. http://www.sciencedirect.com/science/article/pii/S0006349518303497.
68. MacPherson, Q., B. Beltran, and A. J. Spakowitz. 2018. Bottom–up modeling of chromatin segregation due to epigenetic modifications. *Proc. Natl. Acad. Sci. USA.* 115:12739–12744. http://www.pnas.org/content/115/50/12739.abstract.
69. Nuebler, J., G. Fudenberg, …, L. A. Mirny. 2018. Chromatin organization by an interplay of loop extrusion and compartmental segregation. *Proc. Natl. Acad. Sci. USA.* 115:E6697–E6706.
70. Qi, Y., and B. Zhang. 2019. Predicting three-dimensional genome organization with chromatin states. *PLoS Comput. Biol.* 15:e1007024. http://dx.plos.org/10.1371/journal.pcbi.1007024.
71. Huang, K., Y. Li, …, I. Szleifer. 2020. Physical and data structure of 3D genome. *Sci. Adv.* 6:eaay4055.
72. Laghmach, R., M. Di Pierro, and D. A. Potoyan. 2020. Mesoscale liquid model of chromatin recapitulates nuclear order of eukaryotes. *Biophys. J.* 118:2130–2140. http://www.sciencedirect.com/science/article/pii/S0006349519307878.
73. Zhang, B., and P. G. Wolynes. 2017. Genomic energy landscapes. *Biophys. J.* 112:427–433. https://www.ncbi.nlm.nih.gov/pubmed/27692923.
74. Zhang, B., and P. G. Wolynes. 2015. Topology, structures, and energy landscapes of human chromosomes. *Proc. Natl. Acad. Sci. USA.* 112:6062–6067.
75. Latham, A. P., and B. Zhang. 2019. Improving coarse-grained protein force fields with small-angle X-ray scattering data. *J. Phys. Chem. B.* 123:1026–1034.
76. Xie, W. J., and B. Zhang. 2019. Learning the formation mechanism of domain-level chromatin states with epigenomics data. *Biophys. J.* 116:2047–2056. https://doi.org/10.1016/j.bpj.2019.04.006.
77. Lafontaine, D. L. J., J. A. Riback, …, C. P. Brangwynne. 2021. The nucleolus as a multiphase liquid condensate. *Nat. Rev. Mol. Cell Biol.* 22:165–182.
78. Chen, Y., and A. S. Belmont. 2019. Genome organization around nuclear speckles. *Curr. Opin. Genet. Dev.* 55:91–99.
79. Wang, Y., Y. Zhang, …, J. Ma. 2021. SPIN reveals genome-wide landscape of nuclear compartmentalization. *Genome Biol.* 22:36.
80. Safran, S., and I. Rehovot. 1994. Statistical thermodynamics of surfaces, interfaces and membranes. Frontiers in physics. Avalon Publishing. https://books.google.com/books?id=mWUsAAAAYAAJ.
81. Brackley, C. A., B. Liebchen, …, D. Marenduzzo. 2017. Ephemeral protein binding to DNA shapes stable nuclear bodies and chromatin domains. *Biophys. J.* 112:1085–1093. https://doi.org/10.1016/j.bpj.2017.01.025.
82. Söding, J., D. Zwicker, …, J. Kirschbaum. 2020. Mechanisms for active regulation of biomolecular condensates. *Trends Cell Biol.* 30:4–14.
83. Carrero, G., M. J. Hendzel, and G. De Vries. 2006. Modelling the compartmentalization of splicing factors. *J. Theor. Biol.* 239:298–312.
84. Krietenstein, N., S. Abraham, …, O. J. Rando. 2020. Ultrastructural details of mammalian chromosome architecture. *Mol. Cell.* 78:554–565.e7. https://doi.org/10.1016/j.jmb.2020.11.001.
85. Zane, L., F. Chapus, …, T. Misteli. 2017. HiHiMap: single-cell quantitation of histones and histone posttranslational modifications across the cell cycle by high-throughput imaging. *Mol. Biol. Cell.* 28:2290–2302.
86. Farley, K. I., Y. Surovtseva, …, S. J. Baserga. 2015. Determinants of mammalian nucleolar architecture. *Chromosoma.* 124:323–331.
87. Spector, D. L., and A. I. Lamond. 2011. Nuclear speckles. *Cold Spring Harb. Perspect. Biol.* 3:a000646.
88. Boyle, S., S. Gilchrist, …, W. A. Bickmore. 2001. The spatial organization of human chromosomes within the nuclei of normal and emerin-mutant cells. *Hum. Mol. Genet.* 10:211–219. http://www.ncbi.nlm.nih.gov/pubmed/11159939.
89. Liu, Y., L. Nanni, …, G. Ciriello. 2021. Systematic inference and comparison of multi-scale chromatin sub-compartments connects spatial organization to cell phenotypes. *Nat. Commun.* 12:2439.
90. Hildebrand, E. M., and J. Dekker. 2020. Mechanisms and functions of chromosome compartmentalization. *Trends Biochem. Sci.* 45:385–396.

91. Girelli, G., J. Custodio, …, M. Bienko. 2020. GPSeq reveals the radial organization of chromatin in the cell nucleus. *Nat. Biotechnol.* 38:1184–1193.
92. Falk, M., Y. Feodorova, …, L. A. Mirny. 2019. Heterochromatin drives compartmentalization of inverted and conventional nuclei. *Nature.* 570:395–399.
93. Shin, Y., Y. C. Chang, …, C. P. Brangwynne. 2018. Liquid nuclear condensates mechanically sense and restructure the genome. *Cell.* 175:1481–1491.e13. https://doi.org/10.1016/j.cell.2018.10.057.
94. Kim, J., K. Y. Han, …, A. S. Belmont. 2019. Nuclear speckle fusion via long-range directional motion regulates speckle morphology after transcriptional inhibition. *J. Cell Sci.* 132:jcs226563.
95. Jawerth, L., E. Fischer-Friedrich, …, F. Jülicher. 2020. Protein condensates as aging Maxwell fluids. *Science.* 370:1317–1323.
96. Eils, R., D. Gerlich, …, T. Misteli. 2000. Quantitative imaging of pre-mRNA splicing factors in living cells. *Mol. Biol. Cell.* 11:413–418.
97. Khanna, N., Y. Zhang, …, C. Murre. 2019. Chromosome dynamics near the sol-gel phase transition dictate the timing of remote genomic interactions. *Nat. Commun.* 10:2771–2813. https://doi.org/10.1038/s41467-019-10628-9.
98. Eshghi, I., J. A. Eaton, and A. Zidovska. 2021. Interphase chromatin undergoes a local sol-gel transition upon cell differentiation. *Phys. Rev. Lett.* 126:228101. https://doi.org/10.1103/PhysRevLett.126.228101.
99. Walter, J., L. Schermelleh, …, T. Cremer. 2003. Chromosome order in HeLa cells changes during mitosis and early G1, but is stably maintained during subsequent interphase stages. *J. Cell Biol.* 160:685–697.
100. Bronstein, I., Y. Israel, …, Y. Garini. 2009. Transient anomalous diffusion of telomeres in the nucleus of mammalian cells. *Phys. Rev. Lett.* 103:018102.
101. Chubb, J. R., S. Boyle, …, W. A. Bickmore. 2002. Chromatin motion is constrained by association with nuclear compartments in human cells. *Curr. Biol.* 12:439–445.
102. Jiang, Z., and B. Zhang. 2019. Theory of active chromatin remodeling. *Phys. Rev. Lett.* 123:208102.
103. Jiang, Z., Y. Qi, K. Kamat, and B. Zhang. 2022. Phase separation and correlated motions in motorized genome. *J. Phys. Chem. B.* 126:5619–5628. https://doi.org/10.1021/acs.jpcb.2c03238.
104. Ganai, N., S. Sengupta, and G. I. Menon. 2014. Chromosome positioning from activity-based segregation. *Nucleic Acids Res.* 42:4145–4159.
105. Bruinsma, R., A. Y. Grosberg, …, A. Zidovska. 2014. Chromatin hydrodynamics. *Biophys. J.* 106:1871–1881.
106. Ugarte, F., R. Sousae, …, E. C. Forsberg. 2015. Progressive chromatin condensation and H3K9 methylation regulate the differentiation of embryonic and hematopoietic stem cells. *Stem Cell Rep.* 5:728–740.
107. Johnstone, S. E., A. Reyes, …, B. E. Bernstein. 2020. Large-scale topological changes restrain malignant progression in colorectal cancer. *Cell.* 182:1474–1489.e23.
108. Chang, L., M. Li, …, Y. Sun. 2022. Nuclear peripheral chromatin-lamin B1 interaction is required for global integrity of chromatin architecture and dynamics in human cells. *Protein Cell.* 13:258–280.
109. Bronshtein, I., E. Kepten, …, Y. Garini. 2015. Loss of lamin A function increases chromatin dynamics in the nuclear interior. *Nat. Commun.* 6:8044. http://www.nature.com/articles/ncomms9044.
110. Strom, A. R., R. J. Biggs, …, A. D. Stephens. 2021. HP1α is a chromatin crosslinker that controls nuclear and mitotic chromosome mechanics. *Elife.* 10:e63972.
111. Boninsegna, L., A. Yildirim, …, F. Alber. 2022. Integrative genome modeling platform reveals essentiality of rare contact events in 3D genome organizations. *Nat. Methods.* 19:938–949.
112. Shi, G., and D. Thirumalai. 2021. From Hi-C contact map to three-dimensional organization of interphase human chromosomes. *Phys. Rev. X.* 11:011051.

Biophysical Journal, Volume *122*

Supplemental information

Compartmentalization with nuclear landmarks yields random, yet precise, genome organization

Kartik Kamat, Zhuohan Lao, Yifeng Qi, Yuchuan Wang, Jian Ma, and Bin Zhang

Manuscript submitted to **Biophysical** *Journal*

Article

Supporting Information: Compartmentalization with Nuclear Landmarks Yields Random yet Precise Genome Organization

Kartik Kamat[1], Zhuohan Lao[1], Yifeng Qi[1], Yuchuan Wang[2], Jian Ma[2], and Bin Zhang[1,*]

[1]Departments of Chemistry, Massachusetts Institute of Technology, Cambridge, MA 02139, USA
[2]Computational Biology Department, School of Computer Science, Carnegie Mellon University, Pittsburgh, PA, USA
[*]Correspondence: binz@mit.edu

SYSTEM SETUP

The nuclear lamina as a particle-based mesh

The nuclear envelope is a highly complex structure with two lipid membrane and a large number of protein molecules (1). To account for chromatin-lamina interactions while keeping the model simple, we used discrete particles uniformly placed on a sphere to approximate the nuclear lamina. No explicit dynamics was included to account for nuclear deformation, though it could be implemented rather straightforwardly.

The positions of the coarse-grained particles were determined as follows. A straightforward way of generating lamina is by drawing random points uniformly distributed on the surface of the sphere with radius R. Clearly, the process may lead to overlapping lamina particles (or huge gaps in the lamina) and a large number of lamina particles may be required to form a caged network that can contain the chromatin inside the nucleus. Additionally, the generated network is not a strictly reproducible starting point because the lamina configuration depends on the state of the random number generator.

We circumvent these issues by using the Fibonacci grid to initialize the lamina particles that allows a uniform and an almost equidistant network of lamina particles on the surface of the nucleus.(2, 3) The angular coordinates (θ, ϕ) associated with the lamina particles are

$$\begin{aligned}\theta_i &= \frac{\pi}{2} + \sin^{-1}\frac{2i}{2N+1}\\ \phi_i &= 2\pi i \Phi^{-1}\end{aligned} \tag{S1}$$

where $i \in \{-N, -N+1, ..., 0, ..., N-1, N\}$ such that $N_L = 2N+1$ and $\Phi = \frac{1+\sqrt{5}}{2}$ is the golden ratio. The spherical coordinates (R, θ_i, ϕ_i) for an i^{th} lamina particle are finally converted to Cartesian coordinates. We set the radius $R = 13.0\sigma = 5\mu$m. As mentioned in the text, σ is the length unit and is related to the diameter of a chromatin bead ($1\sigma = 385$ nm).

The number of lamina particles (N_L) were chosen such that for every lamina particle there is at least one neighboring lamina particle within a distance of 1σ. The *query_radius* function under the KDTree method available in the scikit library (for Python programming language) was used to identify the neighbors. We determined that 2087 lamina particles are required to meet the aforementioned constraint for a nucleus with radius 13σ.

Nucleoli and speckles as phase-separated droplets

Nucleoli

We fixed the number of nucleolus particles ($N_n = 300$) based on the experimentally reported values of nuclear protein NPM1 concentration as done in a recent study (4).

The size of nucleolar particles (σ_n) was estimated as follows. We accounted for the multi-droplet state of the nucleolus where the typical number of nucleoli experimentally observed within a cell ranges from 2-5. Accordingly, we used a three droplet state as a reference and a space filling approximation within a individual nucleoli droplet (with $N_n/3$ particles)

$$\frac{(4\pi/3)(2^{1/6}\sigma_n/2)^3(N_n/3)}{(4\pi/3)R_N^3} = \left(\frac{R_n}{R_N}\right)^3 \tag{S2}$$

where the subscript N denotes the nucleus and $2^{1/6}\sigma_n/2$ is the effective radius of a nucleoli particle that interacts via a Lennard-Jones potential. For a typical size of the nucleoli of $R_n = 0.5\ \mu$m and $R_N = 13.0\sigma = 5\ \mu$m, the above equation yields $\sigma_n = 0.5$.

Speckles

We estimated the number of speckle particles per cluster using the protein densities calculated from refractive index measurements (5). The relative mass densities of the protein concentrations in the speckle and nucleolus droplet is given by

$$\frac{N \times m/0.3^3}{100 \times m/0.5^3} = \frac{170}{203}, \tag{S3}$$

where we used a speckle radius of 0.3 μm that yields $N \approx 20$. We target 30 speckles in the model to be commensurate with the experimentally reported range of 20-50 speckles. Accordingly, we use a total of 600 speckle particles. Using the speckle radius of 0.3 μm with 20 particles in the droplet in equation S2 yields a $\sigma = 0.5$ for the size of speckle particles.

ENERGY FUNCTION OF THE NUCLEUS MODEL

Hi-C inspired interactions for the diploid human genome

The energy function of the genome model is defined as

$$U_{\text{Genome}}(\mathbf{r}) = U(\mathbf{r}) + U_{\text{sc}}(\mathbf{r}) + U_{\text{ideal}}(\mathbf{r}) + U_{\text{compt}}(\mathbf{r}). \tag{S4}$$

$U(\mathbf{r})$ represents a generic potential applied to each chromosome to ensure the polymeric topology of chromosomes:

$$U(\mathbf{r}) = \sum_i \left[u_{\text{bond}}(r_{i,i+1}) + u_{\text{angle}}(\vec{r}_{i,i+1}, \vec{r}_{i+1,i+2}) \right], \tag{S5}$$

where $u_{\text{bond}}(r_{i,i+1})$ and $u_{\text{angle}}(r_{i,i+1}, r_{i+1,i+2})$ are the bonding and angular potential applied for neighboring beads to ensure the connectivity of the chromatin chain.

$$\begin{aligned} u_{\text{bond}}(r_{i,i+1}) &= -\frac{1}{2}K_b R_0^2 \ln\left[1 - \left(\frac{r_{i,i+1}}{R_0}\right)^2\right], K_b = 30\epsilon, R_0 = 1.5\sigma \\ u_{\text{angle}}(\vec{r}_{i,i+1}, \vec{r}_{i+1,i+2}) &= K_a\left[1 - \cos(\theta - \pi)\right], K_a = 2\epsilon, \cos\theta = \frac{\vec{r}_{i,i+1} \cdot \vec{r}_{i+1,i+2}}{\left|\vec{r}_{i,i+1}\right| \cdot \left|\vec{r}_{i+1,i+2}\right|}. \end{aligned} \tag{S6}$$

The soft-core potential provides excluded volume effects for pairs of beads from the same or different chromosomes

$$U_{\text{sc}}(\mathbf{r}) = \sum_{j>i} u_{\text{sc}}(r_{ij}). \tag{S7}$$

$u_{\text{sc}}(r_{ij})$ is a soft-core potential added to each pair formed by beads index i and j to account for the excluded volume effect while allowing finite probability of cross-over of polymer chains.

$$u_{\text{sc}}(r_{ij}) = \begin{cases} 0.5E_{\text{cut}}\left(1 + \tanh\left[\frac{2U_{\text{LJ}}(r_{ij})}{E_{\text{cut}}} - 1\right]\right), & r_{ij} \le r_{\text{cut}} \\ U_{\text{LJ}}(r_{ij}), & r_{\text{cut}} < r_{ij} \le 2^{1/6}\sigma \\ 0, & r_{ij} > 2^{1/6}\sigma \end{cases} \tag{S8}$$

which corresponds to the Lennard-Jones potential capped off at a finite volume within a replusive core to allow for chain crossing at finite energy cost. $E_{\text{cut}} = 4\epsilon$ and r_{cut} is chosen as the distance at which $U_{\text{LJ}}(r) = 0.5E_{\text{cut}}$.

$U_{\text{ideal}}(\mathbf{r})$ is the intra-chromosomal potential applied to genomic loci within the same chromosome, while $U_{\text{compt}}(\mathbf{r})$ is the compartment-specific interaction potential. The ideal potential adopts the following form:

$$U_{\text{ideal}}(\mathbf{r}) = \sum_I \sum_{i,j \in I} \alpha_{\text{ideal}}(|i-j|) f(r_{ij}) \tag{S9}$$

where I indexes over each chromosome and i and j index over pair of beads on that chromosome. $\alpha_{\text{ideal}}(|i-j|)$ depends only on the sequence separation between two beads i and j. $f(r_{ij})$ measures the probability of contact formation for two loci separated by a distance of r_{ij}, and its ensemble average corresponds to the contact probability measured in Hi-C experiments. $f(r_{ij})$ adopts the form:

$$f(r_{ij}) = \begin{cases} \frac{1}{2}\left[1 + \tanh\left[\eta(r_c - r_{ij})\right]\right], & r_{ij} \le r_c \\ \frac{1}{2}\left(r_c/r\right)^4, & r_{ij} > r_c \end{cases} \tag{S10}$$

Numerical values of r_c and η were determined from imaging data as detailed in the next section. Additionally, it is to be noted that we truncate the ideal potential to be applicable for a sequence separation less than or equal to 100 MB and set the alpha parameters for the higher sequence separations to be zero. This is done because the number of occurrences of bead pairs with sequence separation greater than 100 MB drastically reduces. Incorporating these interactions for improving the model further is straightforward but the resulting model would have higher number of parameters than used in this study.

Similar to the ideal potential discussed above we have

$$U_{\text{compt}}(\mathbf{r}) = \sum_{i,j} \alpha_{\text{compt}}(T_i, T_j) f(r_{ij}) \tag{S11}$$

T_i and T_j denote the compartment types of beads i and j which can be A, B or C.

Mathematical expressions for the various energy terms in $U_{\text{Genome}}(\mathbf{r})$ were designed such that their ensemble averages can be mapped onto combinations of contact frequencies measured in Hi-C. The correspondence between the energy functions and Hi-C measurements allows model parameterization with an efficient maximum entropy optimization algorithm. Specifically, $\alpha_{\text{ideal}}(|i-j|)$ and $\alpha_{\text{compt}}(T_i, T_j)$ were tuned to satisfy the following constraints:

$$\begin{aligned} \left\langle \sum_I \sum_{i,j \in I} f(r_{ij}) \delta_{|i-j|,s} \right\rangle &= \sum_I \sum_{i,j \in I} f_{ij}^{\text{exp}} \delta_{|i-j|,s}, \qquad \text{for } s = 1, \cdots, n-1 \\ \left\langle \sum_{i,j} f(r_{ij}) \delta_{T_i,T_1} \delta_{T_j,T_2} \right\rangle &= \sum_{i,j} f_{ij}^{\text{exp}} \delta_{T_i,T_1} \delta_{T_j,T_2}, \qquad \text{for } T_1, T_2 \in \{A, B, C\} \end{aligned} \tag{S12}$$

where δ_{T_i,T_1} is the Kronecker delta function with the following definition:

$$\delta_{T_i,T_1} = \begin{cases} 1, \text{if } T_i = T_1 \\ 0, \text{otherwise} \end{cases} \tag{S13}$$

The angular bracket represents the ensemble average and f_{ij}^{exp} is the corresponding experimental contact frequency.

We applied an iterative algorithm to derive the values for $\alpha_{\text{ideal}}(|i-j|)$ and $\alpha_{\text{compt}}(T_i, T_j)$ that enforce the constraints defined in Eq. S12. We chose $n = 101$, leading to a total of 100 parameters for $\alpha_{\text{ideal}}(|i-j|)$. Together with the six parameters in $\alpha_{\text{compt}}(T_i, T_j)$, the genome model consists of 106 parameters that are all derived from Hi-C data.

Parameterizing the contact function

The function $f(r)$ defined in Eq. S10 was used to determine the chromatin contact probabilities. These contact probabilities form the basis for optimization as the maximum entropy algorithm iteratively modifies the force field parameters to Hi-C data. Accordingly, it is important to select the parameters r_c and η to be commensurate with experimental data.

A recent study conducted by Su et al. reported the spatial positions of thousands of loci from individual cells of human lung fibroblasts (IMR90) using DNA-MERFISH imaging (6). The availability of both spatial positions and Hi-C data makes possible the definition of a contact function, $f(r)$, that converts distances into contact probabilities. The raw Hi-C contacts were first converted to probabilities by normalizing with the total number of contacts. We apply a Savitzky-Golay filter to these contact probabilities to convert the noisy data to a smooth contact probability function. We re-normalize the smoothed contact probability function such that the it starts from a value of 1.0. We then calculated r_c by identifying the distance where the smoothed contact probability function approaches the value 0.5. Finally, we curve fitted the processed data to the left of r_c with the tanh contact function to define the parameter η. We determined that $r_c = 334$ nm (see figure S23) and $\eta = 0.0117$ nm^{-1}. As discussed previously we used reduced units for our simulations with the conversion $1\sigma = 385$ nm. Accordingly, the r_c and η in reduced units are 0.868 and 4.503 respectively.

SPIN state renormalized chromosome-nuclear landmark interactions

The three nuclear landmarks incorporated in this work are lamina, nucleoli and speckles. Interactions between chromatin and nuclear landmarks were described with the Lennard Jones potential.

We used the following procedure to rescale the interactions between the genome and nuclear landmarks and incorporate specificity. SPIN combines TSA-Seq, DamID data with Hi-C data to partition the chromatin into nine unique states that occupy distinct nuclear regions.(7) It further assigns each chromatin region (25 KB in size) with a probability for being in a particular state. We used these probabilities to denote the likelihood of each chromatin chromatin bead i for interacting with the three nuclear landmarks as P_i^{L}, P_i^{N} and P_i^{S}. The lamina associating probability, P_i^{L}, was determined by accumulating SPIN probabilities for states Lamina, Near_Lm1, Near_Lm2, Interior_Repr1 and Interior_Repr2 SPIN states. All these states were found with significant Lamin-B DamID scores. The nucleolus and speckle associating probabilities, P_i^{N} and P_i^{S}, were based on the Int_Repr2 and Speckle state respectively. The interaction strength ϵ in the Lennard Jones potential was then rescaled by P_i. The base value for ϵ is 0.75, 1.5, and 1.5 for lamina, nucleolus and speckle interactions respectively.

Parameter interpretation and sensitivity analysis

We employed a data-driven mechanistic modeling approach to derive parameters from experimental data. These parameters ensure the biological relevance of simulated nuclear structures. The parameters describe effective interactions among chromatin segments, and between chromatin and nuclear landmarks. For example, intra-chromosomal interactions were approximated with an ideal potential instead of explicitly building in the loop-extrusion model. Similarly, we did not explicitly include chromatin regulators that may promote the contacts among chromatin of similar type and their micro phase separation from other types of chromatin.

A significant advantage of our approach is its simplicity and efficiency. For example, explicitly modeling loop extrusion would require non-equilibrium simulations of Cohesin molecule along the DNA sequence coupled with molecular simulations of the chromosome conformational dynamics (8, 9). Additionally, to ensure the biological relevance of simulated chromosome structures, cohesin extrusion rate, concentration, dissociation rate, and the CTCF permeability, will need to be tuned in a cell type specific manner. An exhaustive search of the parameter space can be computationally demanding. Simulating compartmentalization with molecular details can be equally challenging since the exact set of protein molecules mediating chromatin-chromatin interactions is not fully known. For the known proteins that are involved in chromatin organization, parameters such as protein concentration, protein-protein interaction energy, protein-chromatin interaction energy, remain to be determined. The computational cost for explicitly modeling these additional protein molecules will be high as well. On the other hand, under the theoretical framework of maximum entropy optimization, all parameters for chromatin interactions in our model can be derived uniquely from the Hi-C data. Because they are fixed by experimental measurements, the energy function is deemed effective and accounts for both the physico-chemical interactions between chromatin segments and the contribution of non-equilibrium processes.

Furthermore, parameters in our model are indeed interpretable and consistent with proposed mechanisms of genome organization. A total of 106 tunable parameters were used to describe both intra and inter-chromosomal contacts. This number is rather minimal compared to the millions of contacts detected in Hi-C experiments. Consistent with the knowledge that heterochromatin is more condensed (10), the interactions among B compartments are indeed stronger than that for A compartments (see Table S1). Similarly, values in the ideal potential are mostly negative (see the Excel file), consistent with the formation of cross links by cohesin molecules to favor chromatin segments in close contacts.

Interaction parameters among nuclear body particles. Interactions among nuclear body particles were designed to simplify the resulting model. Parameters were tuned to produce nuclear body numbers comparable to experimental values.

For example, a cut and shifted Lennard-Jones (LJ) potential was used to model the interactions among nucleolus particles, i.e.,

$$U_{\mathrm{LJ}}(r_{ij}) = \begin{cases} 4\epsilon\left(\left(\frac{\sigma}{r_{ij}}\right)^{12} - \left(\frac{\sigma}{r_{ij}}\right)^{6}\right) - E_{\mathrm{cut}} & \text{for } r <= r_{\mathrm{cut}} \\ 0 & \text{for } r > r_{\mathrm{cut}} \end{cases}, \tag{S14}$$

with $E_{\mathrm{cut}} = 4\epsilon\left(\left(\frac{\sigma}{r_{\mathrm{cut}}}\right)^{12} - \left(\frac{\sigma}{r_{\mathrm{cut}}}\right)^{6}\right)$. The two parameters σ and ϵ in this potential were determined based on the average size of nucleoli and an average of two nucleoli per cell. In a previous study (4), we carried out systematic explorations of the parameter space and found that weakening the interactions results in the dissolution of nucleoli, while increasing the strength can cause the formation of more nucleoli.

A simple LJ potential cannot produce the desired number of speckles over a large range of parameter values (Figure S3). This observation motivated our use of a linear super-position of the LJ (Eq.S14) and the Yukawa potential (11) given by

$$U_{\mathrm{Sp}}(r_{ij}) = U_{\mathrm{LJ}}(r_{ij}) + \left(A\frac{e^{-\kappa r_{ij}}}{r_{ij}} - U_{\mathrm{cut}}^{\mathrm{Yuk}}\right), \tag{S15}$$

where $U_{\mathrm{cut}}^{\mathrm{Yuk}} = Ae^{-\kappa r_{\mathrm{cut}}^{\mathrm{Y}}}/r_{\mathrm{cut}}^{\mathrm{Y}}$. This Yukawa potential can account for long-range electrostatics that may arise due to the charges present in RNA and protein molecules. As discussed in the *Section: Non-equilibrium model for speckle formation*, it may further approximate non-equilibrium mechanisms that suppress the coarsening. The three parameters ϵ, χ, and A were tuned to produce speckle numbers on the order of 30-40 (12, 13). As shown in Figure 5 of the main text, varying the value of χ causes dramatic changes in the speckle number.

Interaction parameters between chromatin and nuclear landmarks. For simplicity, we set the parameter in the LJ potential between chromatin and nucleoli the same as that between nucleolus particles. In a previous study (4), we found that the interaction strength between nucleoli and chromatin also affects the number of nuclear bodies and stronger interactions can lead to more nucleoli. The same parameter was also adopted for the LJ potential between chromatin and speckle particles. Varying this parameter within a reasonable range does not significantly impact the agreement between simulated and experimental TSA-Seq profiles(Figure S2B).

When using the same parameter for chromatin-lamina interactions, we found a poor agreement between simulated and experimental DamID profiles. Therefore, we varied ϵ in the LJ potential to find the optimal value that produces the best agreement between simulation and experiment DamID profiles (See Figure S2).

Perturbing chromatin-nuclear landmark interactions. As mentioned in the *Section: SPIN state renormalized chromosome-nuclear landmark interactions*, we normalized the interaction strength with probabilities estimated from SPIN states. These probabilities account for the presence of multiple different types of small chromatin domains that coexist in a one MB bead. To test the role of the probabilistic assignment on reproducing chromatin-nuclear body contacts, we explored a model that adopts a binary classification for the three states. This binarization was done by converting the SPIN annotation probabilities into 0 or 1 (with 0.5 threshold) such that each chromatin bead is now either completely interacting or non-interacting with speckles, lamina, or nucleoli. As shown in Figure S1, removing the probabilistic assignment significantly deteriorated the agreement between simulated and experimental DamID profiles. However, the agreement between TSA-Seq data was relatively unaltered. The differential behavior arises since most of the speckle associating domains are comparable to the size of the coarse grained bead. However, the size of lamina associating domains is much more heterogenous and the probabilistic assignment is crucial for capturing the difference among them.

Chromatin-lamina interactions. Nuclear lamina plays important role in genome function, and mutations found in lamin proteins are frequently implicated in diseases. To study how chromatin-lamina interactions affect genome organization, we performed additional simulations that removed the interactions between the chromatin and the lamina, i.e., by $\epsilon_{\text{chr-lamina}} = 0$ (Table S2). As shown in Figure S19 A and B, the ensemble of structures from such a model completely loses its capacity to reproduce LaminB1 DamID experimental data. Additionally, the simulated structures do not agree with experimental radial positions of chromosomes (see Figure S19C). Our simulation results are consistent with several recent experimental studies that observed significant LAD dissociation from the nuclear envelope in cells with depleted lamin proteins (14–16). We note that, in addition to passive interactions, non-equilibrium mechanisms could contribute to the spatial organization of chromatin, as shown in Ref. (17). It is possible that disrupting lamin proteins alone is not sufficient to completely abolish the preferential localization of certain chromatin at the nuclear periphery (18, 19).

We predicted that the chromatin dynamics is increased in the perturbed model. We quantified the increase by calculating the mean squared displacement of the chromatin beads and computing the resulting change in diffusion coefficients (see Figure S20). Our model predicts a 63% slower diffusion coefficient for the normal cell than the depleted lamina cell. A slow down of similar magnitude was observed by Chang et al. when comparing chromatin dynamics of normal cells with the LaminB1 protein depleted cell (16).

Chromatin-speckle interactions. We ran simulations with removed interactions between chromatin and speckles/nucleoli by setting $\epsilon_{\text{chr-speckle/nucleoli}} = 0$ (Table S2). Not surprisingly, the resulting genome structures fail to produce TSA-seq profiles that match experimental values (see Figure S21). However, this perturbation does not significantly alter chromatin-lamina interactions. Together with results shown in Figure S19 A and B, these simulations support a decoupling between two nuclear landmarks, lamina and speckles. Their interactions with chromatin are relatively independent of each other.

Surprisingly, removing chromatin-speckle interactions does not impact the radial positions of chromosomes. The agreement between simulated and experimental chromosome positions is preserved even after removing the compartmentalization force, i.e., by setting α_{compt} defined in Eq. S10 to zero. Therefore, chromatin lamina interactions largely dictate the radial positions of individual chromosomes.

Chromatin speckle interactions are also key for giving rise to heterogeneity of genome organization and viscoelastic behaviors of chromatin. As shown in Figure S16, upon removing these interactions, the heterogeneity among A1-A1 contacts across trajectories almost vanished, and the system can equilibrate these contacts on simulation timescales.

We further computed the complex modulus of chromatin with and without the presence of speckle interactions, and observed a significant difference in the relaxation timescales. As shown in Figure S18, chromatin exhibits multiple timescales and behaves as a viscoelastic network. The crossover at longtimescales between $G'(t)$ and $G''(t)$ signifies the transition from gel to liquid. Upon removing chromatin speckle interactions, we found that all the four timescales τ_n decreased (see Eq. S26), supporting the role of speckles in chromatin dynamics.

To our surprise, the longest timescale does not completely disappear upon removing speckles. We further computed the shear relaxation modulus for simulations that abolished chromatin-lamina interactions. As shown in Figure S18 a significant decrease in the longest relaxation timescale is observed.

Our simulation results are consistent with the experimental observations of significantly enhanced chromatin dynamics upon depleting lamina A (20). Perturbing lamina A has been shown to both alter chromatin speckle (21) and chromatin lamina interactions. Future experiments that more specifically address chromatin-nuclear landmark interactions could further elucidate contributions of various components to chromatin dynamics.

MOLECULAR DYNAMICS SIMULATION DETAILS

Initializing simulations with randomly places chromosomes

The results presented in the main text were produced from simulations initialized with chromosome configurations obtained from a separate sampling of a genome model introduced in a previous study (22). To explore the sensitivity of these results with respect to initial configurations, we ran 12 independent simulations with configurations of the chromosomes initialized randomly. We briefly highlight the procedure we used for the randomization. The first bead of the chromosome is initialized at the origin (center of the nucleus model). This is followed by generating a vector that is uniformly distributed on the surface of a unit sphere, with the center of the sphere corresponding to the first bead. Scaling this vector with the expected bond distance between the beads (1σ) yields the Cartesian coordinates of the next bead. We repeat the procedure for all the subsequent beads within the chromosome, and the Cartesian coordinate of the subsequent bead is only accepted if the radial distance from the origin is less than 4σ (so as to randomly initialize them as globules). The procedure is similar across all the chromosomes. Lastly, we shift the chromosomes such that their center of masses are at random locations inside the nucleus.

Perturbing speckle numbers

We modified the number of speckles in the system by perturbing the interaction parameters of speckles to study the resulting effect on A compartment organization. As discussed earlier, the 36 speckle cluster system discussed in the main text is stabilised through the Yukawa repulsion potential with $\chi_0 = 0.95$. To perturb the number of speckles we ran simulations with χ equal to $0.8\chi_0$ and $0.9\chi_0$ that resulted in a 10 and 20 speckle system respectively.

Modeling the genome at the 100 KB resolution

We further carried out simulations of the 100 KB resolution model to study nuclear organization. The finer resolution results in an increase of particles by a factor of 10 and the model is computationally more costly. To avoid long relaxation that's required to reach equilibrium, we initialized simulations using configurations predicted by the 1MB resolution model. In particular, we increased the resolution of the model by linear interpolation between every two 1MB particles. The number of speckle, nucleus, and lamina particles was kept the same. We then performed a brief minimization before launching equilibrium simulations.

We adjusted the energy function for improved simulation stability and to account for the increased resolution. The bond potential in Eq. S6 was modified to a less stiff potential as

$$u_{\mathrm{bond}}(r_{i,i+1}) = K_2(r-r_0)^2 + K_3(r-r_0)^3 + K_4(r-r_0)^4 \tag{S16}$$

with $r_0 = 0.5$ and $K_2 = K_3 = K_4 = 20.0$. The soft-core potential in Eq. S7 was changed to

$$u_{\mathrm{sc}}(r_i) = A[1+\cos(\frac{\pi r}{r_c})] \tag{S17}$$

with $A = 10.0$, $r_c = 0.56$. We also rescaled the pair-wise interactions $U_{\mathrm{ideal}}(\mathbf{r})$ and $U_{\mathrm{inter}}(\mathbf{r})$ by a factor of 0.01 to account for almost 100 times more contacts when increasing the model resolution from 1MB to 100KB. To prevent non-lamina beads from moving outside the nuclear envelope, we added a WCA potential with the form

$$U_{\mathrm{wall}}(r) = \begin{cases} 4\epsilon[(\frac{\sigma}{r})^{12} - (\frac{\sigma}{r})^{6}] + E_{\mathrm{cut}}, & r < r_c \\ 0, & \text{otherwise,} \end{cases} \tag{S18}$$

where E_{rm} is the energy of the LJ potential at the cutoff distance $r_c = 2^{1/6}\sigma$.

We estimated the size of 100 KB beads as 192 nm based on super-resolution imaging data, which was converted to 0.5σ in the reduced unit.

We performed 23 independent 800000-step-long simulations to compute simulated DamID and TSA-Seq profiles. As shown in Figure S7, we found that the 100kb model provides a better representation of the various chromatin domains. In particular, for DamID profiles, simulation results now better captures the heterogeneity of enrichment in lamina-associated domains, as evidenced by the more pronounced fluctuations compared to that shown in Figure 3 of the main text. To our surprise, however, the genome-wide average Pearson correlation coefficient between simulated and experimental DamID/TSA-Seq profiles is not significantly improved in the 100kb model. Further improving the agreement potentially require going beyond SPIN state based modeling strategy and would be an interesting direction for future exploration.

Non-equilibrium model for speckle formation

When modeling speckles, we introduced the Yukawa potential with a long-range repulsion between the coarse-grained speckle particles. This potential approximates the electrostatic repulsion among RNA and protein molecules and the impact of chemical modifications on proteins, both of which can suppress droplet coarsening (23). This approximation suffices for stabilizing the multidroplet state, but cannot fully capture the fusion kinetics of speckles. However, the central aim of this study was to incorporate the effects of nuclear landmarks such as speckles on chromatin and not to capture the complete physico-chemical behavior of speckles. We believe that conclusions on the nuclear organization should be insensitive to the scheme used to model the details of speckle clusters.

To examine whether the effective equilibrium model for speckles introduces any biases on our conclusions of genome organization, we tested a kinetic scheme of speckle formation introduced by de Vries and coworkers (23). In this scheme, we consider two types of speckle molecules: phosphorylated (P) and de-phosphorylated (dP). The two types can inter-convert via chemical reactions with rates ρ and σ, and only dP particles share attractive interactions with each other. For simplicity, we set $\rho = \sigma = 0.0694\ \text{s}^{-1}$ which compare well with experimental values.(24) dP particles interact with chromatin segments through SPIN states as discussed previously. The *fix atom/swap semi-grand* functionality within the LAMMPS simulation package was used to swap P and dP particles on the fly, while keeping the total speckle particles constant. We increased the total number of speckle particles to 1512 to produce approximately 30-50 droplets upon reaching the steady state.

As shown in Figure S4, this model succeeds in suppressing droplet coarsening, producing an average of 45 speckles in individual simulations. The simulated TSA-seq profiles also agree well with experimental profiles (Figure S4C). Notably, the non-equilibrium model for speckles reproduced the two important features of genome organization, disordered and precise contacts. As shown in Figure S4D, there are significant fluctuations among "contacting" $A1$ segments that are bound to the same speckle across simulation trajectories. On the other hand, contacts among $A1$ evaluated at different time points of the same trajectory are relatively robust with minimal changes. These results are remarkably similar to the ones presented in Figure 6 of the main text. Therefore, we conclude that the effective model presented in the main text indeed provides a good approximation to the role of speckles on genome organization.

DETAILS ON ANALYSIS AND VALIDATION

Computing simulated contact maps

In this section, we discuss the details of calculating the simulated Hi-C maps. For two chromatin segments (say i and j) we use the contact function defined in Eq. S10 to enumerate a contact between them. The contacts between these segments are monitored over different frames and trivially ensemble averaged. Thus, one trajectory yields one Hi-C contact matrix. We run several independent trajectories (starting from distinct initial configurations) and average the contact matrices across trajectories to yield an ensemble averaged Hi-C contact matrix (for e.g. as reported in Figure 3A of the main text).

Distances from nuclear bodies and association frequencies

In this section we discuss in detail the procedure used to calculate distances and associations with the nuclear landmarks. The center of the spherical nucleus is located at the origin and hence the Cartesian coordinates of a bead i readily yieds the radial position r_i. As the lamina is located exactly at $R = 13.0\sigma$, the distance from the lamina ($d_{i,\text{lam}}$) is defined as $R - r_i$.

For calculating distances from the nucleoi and speckles, we first identify clusters of the nuclear bodies. Accordingly, we use the density-based spatial clustering algorithm DBSCAN(25) as implemented in the scikit library for Python. The procedure is same for nucleoi and speckles and we describe the procedure for speckles in the following lines. The algorithm is used to return cluster labels in order to identify all the speckle particles belonging to the same cluster. This information is used to calculate the center of mass of cluster and the radius of gyration of the cluster which is treated as a proxy for the radius of the cluster. The distance of a bead i from a speckle is

$$d_{i,s} = \|\vec{r}_i - \vec{r}_s^{\,com}\| - R_s \tag{S19}$$

where the subscript s denotes the speckle, and the radius of the speckle cluster is subtracted from the distance of the bead to the cluster center of mass. Clearly, bead i will have an array of speckle distances where the length of the array is the number of speckle clusters in the nucleus. We use the minimum distance in this array for calculations shown in Figure 4 of the main text. The procedure is the same for nucleolus clusters.

For a particular frame of a simulation trajectory we define associations with lamina using a heaviside contact function. Thus, the lamina association frequency of a bead i is

$$\mathrm{LAF}_i = \frac{1}{N_t}\sum_t \Theta(d_c - d_{i,\mathrm{lam}}) \tag{S20}$$

where $d_c = 1.5\sigma$ and the subscript t and N_t account for averaging over all the frames of the trajectory. Additionally, we convert the diploid simulation data into haploid by averaging over the homologs. Thus, the model DamID value for the bead i is given by

$$\mathrm{DamID}_i = \log_2\Big(\frac{\mathrm{LAF}_i}{\overline{\mathrm{LAF}}}\Big) \tag{S21}$$

where $\overline{\mathrm{LAF}}$ is the genome-wide average of the lamina association frequencies. We calculated the genome-wide DamID correlation between model prediction and experiment as reported in Figure 3 of the main text.

The model prediction of TSA-Seq uses the exponential decay function associated with speckle distances. As described previously, a bead i has an array of distances from speckles each element denoted by $d_{i,s}$. Thus, the TSA-Seq signal for the genomic bead i is

$$\mathrm{signal}_i = \frac{1}{N_t}\sum_t\sum_s e^{-l_D d_{i,s}} \tag{S22}$$

where we sum over all the speckles and frames in the trajectory and normalize by the number of frames. The parameter l_D denotes the decay length and is set to 4.0 $\mu\mathrm{m}^{-1}$ as determined from the previously reported fit to microscopy data of TSA-Seq experiments.(26) We average the signal for homologs and the model value of TSA-Seq for bead i is

$$\mathrm{TSA_i} = \log_2\Big(\frac{\mathrm{signal_i}}{\overline{\mathrm{signal}}}\Big) \tag{S23}$$

where the denominator is the genome wide average of the TSA-Seq signals.

Shear relaxation modulus of chromatin

To characterize the viscoelastic properties of chromatin, we computed the shear relaxation modulus $G(t)$ using the Green-Kubo formula

$$G(t) = \frac{V}{k_BT}\left\langle \sigma_{\alpha,\beta}(t)\sigma_{\alpha,\beta}(0)\right\rangle, \quad \alpha \neq \beta, \tag{S24}$$

where $\sigma_{\alpha,\beta}$ is the stress tensor. V, k_B and T correspond to the volume, Boltzmann constant and the temperature of the system, respectively, and the Greek subscripts denote the Cartesian coordinates. We further averaged over different combinations for improved statistics with the following formula:

$$\begin{aligned} G(t) = {} & \frac{V}{5k_BT}[\left\langle\sigma_{x,y}(t)\sigma_{x,y}(0)\right\rangle + \left\langle\sigma_{x,z}(t)\sigma_{x,z}(0)\right\rangle + \left\langle\sigma_{y,z}(t)\sigma_{y,z}(0)\right\rangle] \\ & + \frac{V}{30k_BT}[\left\langle N_{x,y}(t)N_{x,y}(0)\right\rangle + \left\langle N_{x,z}(t)N_{x,z}(0)\right\rangle + \left\langle N_{y,z}(t)N_{y,z}(0)\right\rangle] \end{aligned} \tag{S25}$$

where $N_{\alpha,\beta}(t) = \sigma_{\alpha,\alpha} - \sigma_{\beta,\beta}$. We used 50 10-million-step-long simulation trajectories initialized from different configurations to compute the shear relaxation modulus. Configurations were saved at every 10 steps.

We used the Fourier transformation to determine the storage (G') and loss (G'') modulus from $G(t)$ as follows. We fitted $G(t)$ using the generalized Maxwell model as

$$G(t) = \sum_n G_n \exp(-\frac{t}{\tau_n}), \tag{S26}$$

where G_n and τ_n represent the amplitude and relaxation time of the n-th mode. We used $n = 4$, and larger n values do not improve goodness of fit. With the generalized Maxwell model, the storage and loss modulus were computed as

$$\begin{aligned} G' &= \sum_n G_n \frac{(\omega\tau_n)^2}{1 + (\omega\tau_n)^2} \\ G'' &= \sum_n G_n \frac{\omega\tau_n}{1 + (\omega\tau_n)^2} \end{aligned} \tag{S27}$$

Dynamical fluctuation of two different LADs.

Previous experimental studies have revealed two types of lamina-associated domains (LADs): constitutive and facultative. Constitutive LADs (cLADs) are cell-type invariant, while facultative LAD (fLADs) only interact with the NL in certain cell types. It has been speculated that cLADs collectively may form a structural “backbone”, tethering chromosomes to the NL at specific positions and thereby guiding the overall folding of interphase chromosomes. Falsifying this hypothesis has been challenging due to the lack of single-cell data until recently.

We attempted to resolve the differential behavior of cLADs and fLADs by examining the fluctuation in contact to the nuclear lamina using both simulated and imaging data. We collected the lamina distances of cLAD segments from imaging data, resulting in a $N_{cells} \times N_{cLADs}$ matrix. N_{cells} denotes the number of cells studied in the experiment, and N_{cLADs} denotes the number of cLAD segments. We calculated the standard deviation in the cLAD-lamina distances (i.e., fluctuations between cells) by computing the standard deviation over the N_{cells} axis. The resulting data is one-dimensional with length N_{cLADs}. We histogram this data, and cLADs data is shown by green distribution in the upper panel of Figure S10B. The procedure is repeated on the imaging data set to isolate the fluctuation in fLADs. The mean value of such distributions shown in Figure S10B yields the average size of LADs fluctuation, while the standard deviation of the distribution is a measure of the variability between the fluctuations of different LAD segments (fluctuation in fluctuations!). We repeat the process for the simulation data.

The mean value of the fluctuations for cLADs and fLADs computed from imaging data is $0.34 \pm 0.01\mu m$ and $0.35 \pm 0.02\mu m$, respectively. They agree with the mean fluctuation value of $0.55\mu m$ and $0.63\mu m$ predicted from simulations. Therefore, both data support that cLADs contacts with lamina are more stable, while fLADs can be more dynamic with larger fluctuations.

We note that a perfect agreement between simulated and experimental data is difficult to achieve at this point. Part of the discrepancy could be due to the approximate nature of our model. However, two additional aspects inherent to the experimental setup and data collection can also lead to the observed deviations. For example, the experimental nuclei adopt ellipsoidal shapes, with a height of 1.6 μm in the z axis compared to the 7.0 μm and 12.7 μm in the x and y axis respectively. Unlike the spherical nucleus used in simulations, this uneven shape will force most chromatin to be closer to the nuclear lamina. Furthermore, Zhuang et al. did not directly probe the nuclear lamina but approximated the boundary with a convex hull of the imaged chromatin data. This ignores the width of the nuclear envelope, leading to an underestimation of chromatin-lamina distances.

Subcompartment analysis of simulated contact maps.

Although the clustering method we used is the same as done by Rao et al., we discuss the process briefly for clarity.(27) From the simulated genome-wide contact map, we generate a subset contact matrix. In this contact matrix, the genomic segments on the odd-chromosomes appear as rows and the genomic segments on the even-chromosomes are the columns of the matrix. Chromosome X was left out from this analysis. Accordingly, to cluster A compartments on a particular odd chromosome we isolate complete rows that correspond to loci belonging to the chromosome and defined as type A in our model. The process is similar for even-chromosomes except that the subset contact matrix is transposed in this case before isolating A loci. The previous filtering yields a matrix, that is converted into z-scores by passing the rows through Python’s *scipy* z-score function. This is used as the input for a Gaussian hidden Markov model (GaussianHMM) to cluster the A compartment z-scores data into two clusters. Clearly, the clustering procedure returns one of two labels (say 0 and 1) for all the A loci on a particular chromosome without conveying if 0 is related to $A1$ or $A2$. Thus, the procedure returns an array of labels (0s and 1s) for the A loci on a chromosome. To compare with the experimental annotations we use the higher of $A1/A2$ experimental probabilities on a 1 MB A loci to classify the loci as either $A1/A2$ as inferred from the experiment. We set the experimental $A1$ as 0 and $A2$ as 1 to yield an array with 0s and 1s for A loci. This labels array from the experiment is compared to the labels array from the clustering and its binary complement (as label 0 in clustering may not relate to $A1$). The element-wise match between the two label arrays divided by the total number of elements is defined as the overlap between clustering and experimental annotations. The maximum value of the overlap is used to identify subcompartments in clustering and reported in this study.

α_{AA}	-1.441575
α_{AB}	-0.764335
α_{AC}	-0.690723
α_{BB}	-1.507070
α_{BC}	-0.939463
α_{CC}	-0.246267

Table S1: Summary of compartment-compartment interaction parameters, i.e. α_{compt} defined in Eq. S11, used in the study.

$\epsilon_{\text{chr-lamina}}$	0.75
$\epsilon_{\text{chr-nucleolus}}$	1.5
$\epsilon_{\text{chr-speckles}}$	1.5
$\sigma_{\text{chr-lamina}}$	1.0
$\sigma_{\text{chr-nucleolus}}$	0.75
$\sigma_{\text{chr-speckles}}$	0.75

Table S2: Summary of chromatin-nuclear landmark Lennard Jones interaction parameters, i.e. ϵ and σ, used in the study.

Potentials	Functional forms	Parameter values
Bonding potential	$u_{\text{bond}}(r_{i,i+1})$ in Eq. S6	Standard values in coarse-grained polymer models
Angular Potential	$u_{\text{angle}}(\vec{r}_{i,i+1}, \vec{r}_{i+1,i+2})$ in Eq. S6	Standard values in coarse-grained polymer models
Soft-core potential	$u_{\text{sc}}(r_{ij})$ in Eq. S8	Standard values in coarse-grained polymer models
Ideal potential	$U_{\text{ideal}}(\mathbf{r})$ in Eq. S9	Values for α_{ideal} were obtained from optimizations against Hi-C data (see Figure S24).
Compartment potential	$U_{\text{inter}}(\mathbf{r})$ in Eq. S11	Values for α_{compt} were obtained from optimizations against Hi-C data (see Table S1).

Table S3: Summary of the potentials applied to coarse-grained beads representing the genome at the one MB resolution. The bonded energy terms, including the bonding and angular potentials, were applied to consecutive beads on the same chromosome. The ideal potential was also limited to bead pairs from the same chromosome. The non-bonded soft-core potential, and compartment potential were applied to bead pairs both from the same and from different chromosomes. See also Section: Hi-C inspired interactions for the diploid human genome for details on the definition and parameterization of the potential energies.

Potentials	Function forms	Parameter values
Nucleolus-Nucleolus	$U_{\text{LJ}}(r_{ij})$ in Eq. S14	$\epsilon = 2.0, \sigma = 0.5, r_{\text{cut}} = 2.0$, and their values were chosen based on the average size of nucleoli and an average of two nucleoli per cell
Speckle-Speckle	$U_{\text{Sp}}(r_{ij})$ in Eq. S15	$\epsilon = 8.0, \chi = 0.95, \kappa = 1/\chi, A = 2.5\chi$ were chosen to reproduce speckle numbers observed in microscopic images. $r_{\text{cut}} = 2.0,\ r^{\text{Y}}_{\text{cut}} = 6.0\chi,\ \sigma = 0.5$
Nucleolus-Speckle	$U_{\text{LJ}}(r_{ij})$ in Eq. S14	$\epsilon = 1.0, \sigma = 1.0$ were chosen as standard values to provide excluded volume effect. $r_c = 2^{1/6}\sigma$
Nucleolus-Lamina	$U_{\text{LJ}}(r_{ij})$ in Eq. S14	$\epsilon = 1.0, \sigma = 1.0$ were chosen as standard values to provide excluded volume effect. $r_c = 2^{1/6}\sigma$
Speckle-Lamina	$U_{\text{LJ}}(r_{ij})$ in Eq. S14	$\epsilon = 1.0, \sigma = 1.0$ were chosen as standard values to provide excluded volume effect. $r_c = 2^{1/6}\sigma$

Table S4: Summary of the interaction potential among particles that make up the nuclear landmarks. As their names indicate, the Nucleoli-Nucleoli potential was applied to pairs of beads identified as nucleolar particles, and the Speckle-Speckle potential was applied to pairs of beads identified as Speckle particles. The remaining three potentials were applied to particles from two different nuclear landmarks as specified in their respective names.

Potentials	Functional forms	Parameter values
Chromatin-Nucleolus	$U_{\text{LJ}}(r_{ij})$ in Eq. S14	$\epsilon = P_i^{\text{N}}\epsilon_0, \sigma = 0.75$, with $\epsilon_0 = 1.5$. $r_{\text{cut}} = 4.0$.
Chromatin-Speckle	$U_{\text{LJ}}(r_{ij})$ in Eq. S14	$\epsilon = P_i^{\text{S}}\epsilon_0, \sigma = 0.75$, with $\epsilon_0 = 1.5$. $r_{\text{cut}} = 4.0$.
Chromatin-Lamina	$U_{\text{LJ}}(r_{ij})$ in Eq. S14	For non-zero P_i^{L} values, $\epsilon = P_i^{\text{L}}\epsilon_0, \sigma = 1.0$, with $\epsilon_0 = 0.75$. $r_{\text{cut}} = 4.0$. If $P_i^{\text{L}} \equiv 0$, we have $\epsilon = 0.75$ and $r_c = 2^{1/6}\sigma$ to provide excluded volume effects that confine chromatin inside the nucleus.

Table S5: Summary of the non-bonded interactions between genomic beads at one MB resolution and various nuclear landmark particles. P_i^{N}, P_i^{S}, and P_i^{L} represents the probability for a chromatin bead to be in the nucleolus, speckle, and lamina state as assigned by the SPIN algorithm. As mentioned in the main text, SPIN annotates chromatin based on their relative position with respect to various nuclear structures through an integrative analysis of SON TSA-Seq, Lamin B DamID, and Hi-C data (7).

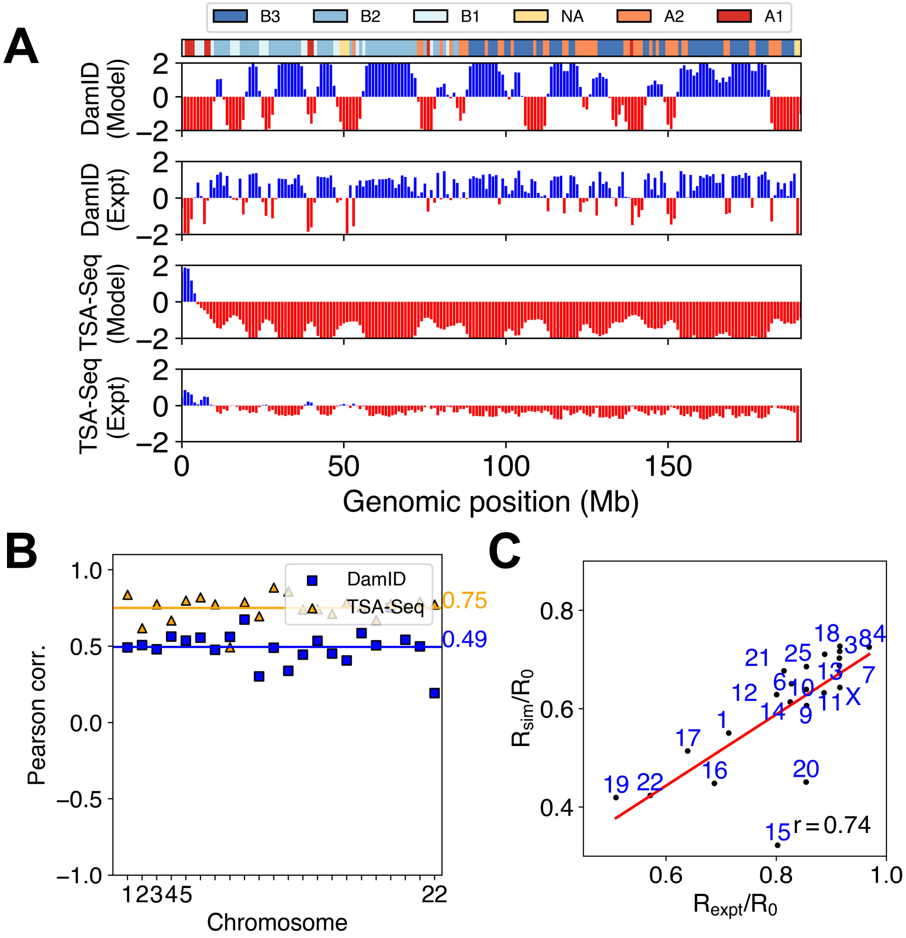

Figure S1: **Probabilistic assignment of chromatin domains helps to account for the heterogeneity of chromatin content.** See text *Perturbing chromatin-nuclear landmark interactions* for additional discussion. (A) Comparison (for chromosome 4) between the model predicted Lamin-B DamID and SON TSA-Seq signals and the experimental data at 1MB resolution. (B) Pearson correlation coefficients between simulated and experimental Lamin-B DamID (blue) and SON TSA-Seq (yellow) data for individual chromosomes. The genome-wide averages are shown as straight lines with the corresponding values on the side. (C) Comparison of the chromosome radial positions in experiment (28) and simulations. Here R_0 is the radius of the nucleus and $R_0 = 13\sigma = 5\mu$m.

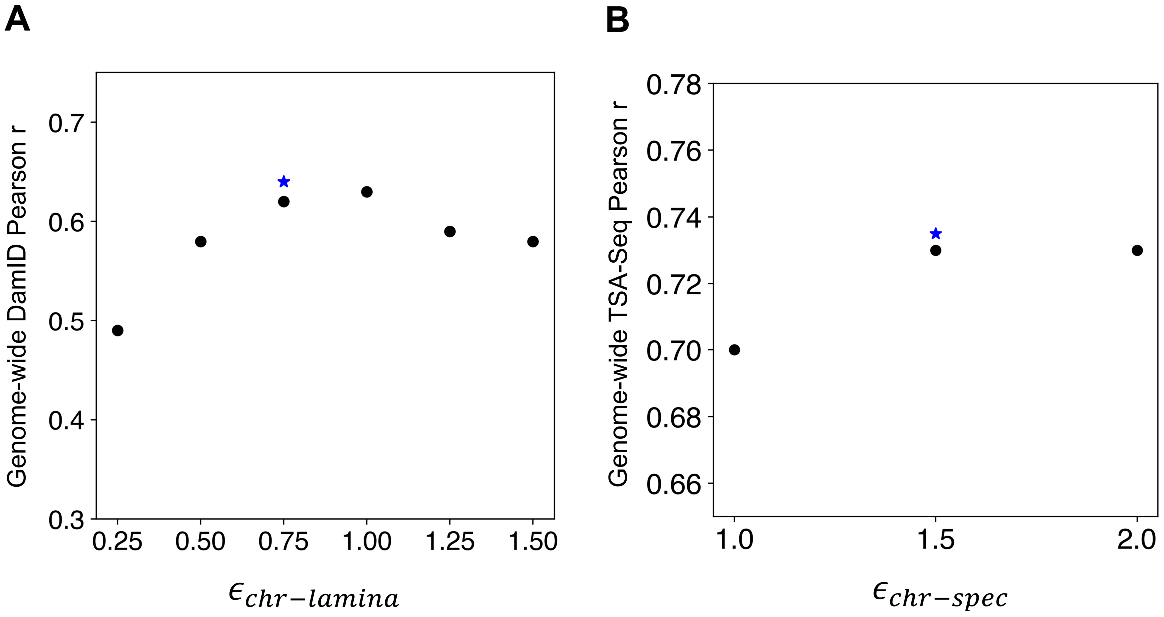

Figure S2: **Varying the interaction parameters in the model for optimal agreement with experimental measurements.** (A) Variation in the genome wide Pearson r correlation between model and experimental DamID profiles on changing the interaction strength of the chromatin-lamina interaction. We clearly observe an optimum in the correlation and the $\star$ symbol denotes the value we used. (B) A similar calculation for the agreement with TSA-Seq data on changing the interaction strength of the chromatin-speckle interaction.

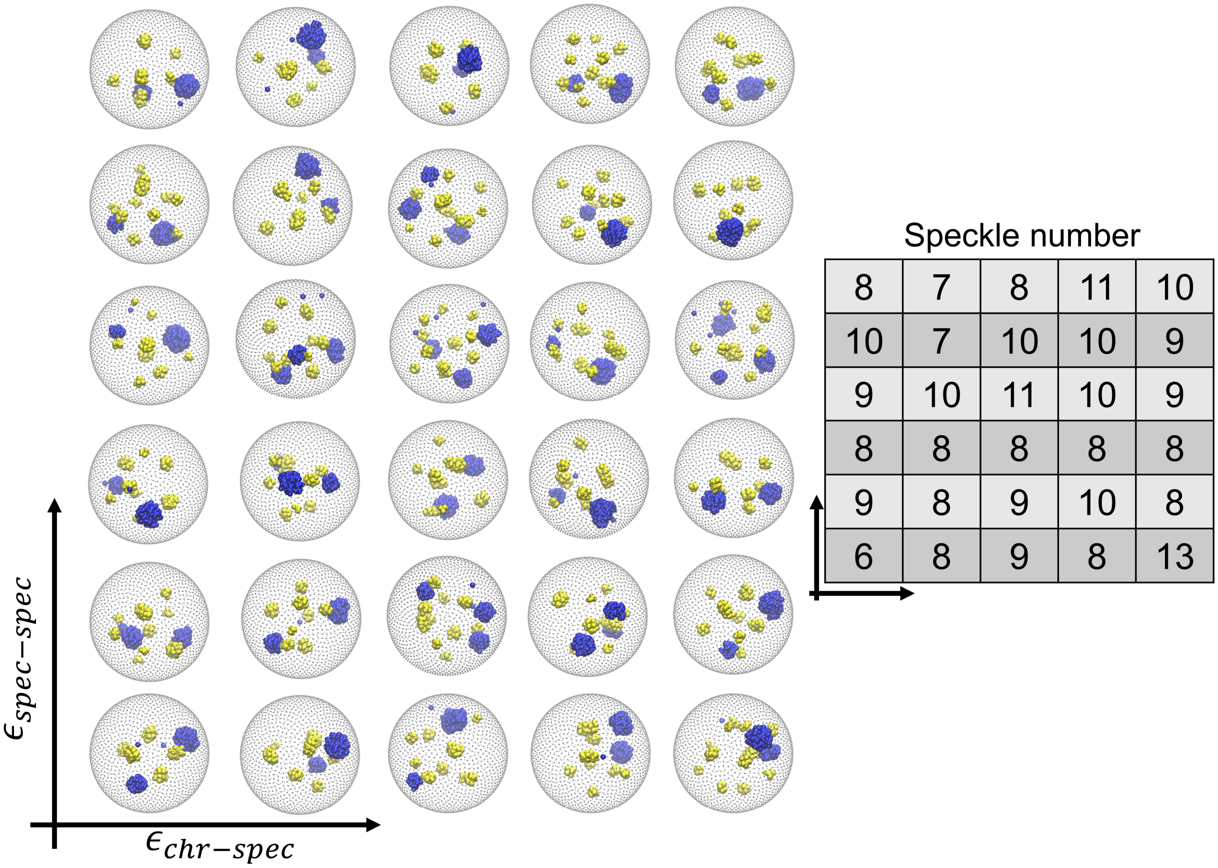

Speckle number

8	7	8	11	10
10	7	10	10	9
9	10	11	10	9
8	8	8	8	8
9	8	9	10	8
6	8	9	8	13

Figure S3: **Dependence of speckle numbers on a model with only attractive interactions.** As discussed in detail in the main text, we observed that a simple model with attractive interactions between speckles (Eq. 2 of main text) is insufficient to yield the experimentally observed number of speckles (30-40). This figure shows the nuceloi (blue) and speckles (yellow) in the last frame of 30 simulations where we varied the epsilon of chromatin-speckle (3.5-5.5 with 0.5 increments) and speckle-speckle interaction (1.2-2.2 with 0.2 increments). Each trajectory is 6 million timesteps. The table summarizes the number of speckle clusters identified using the DBSCAN algorithm.

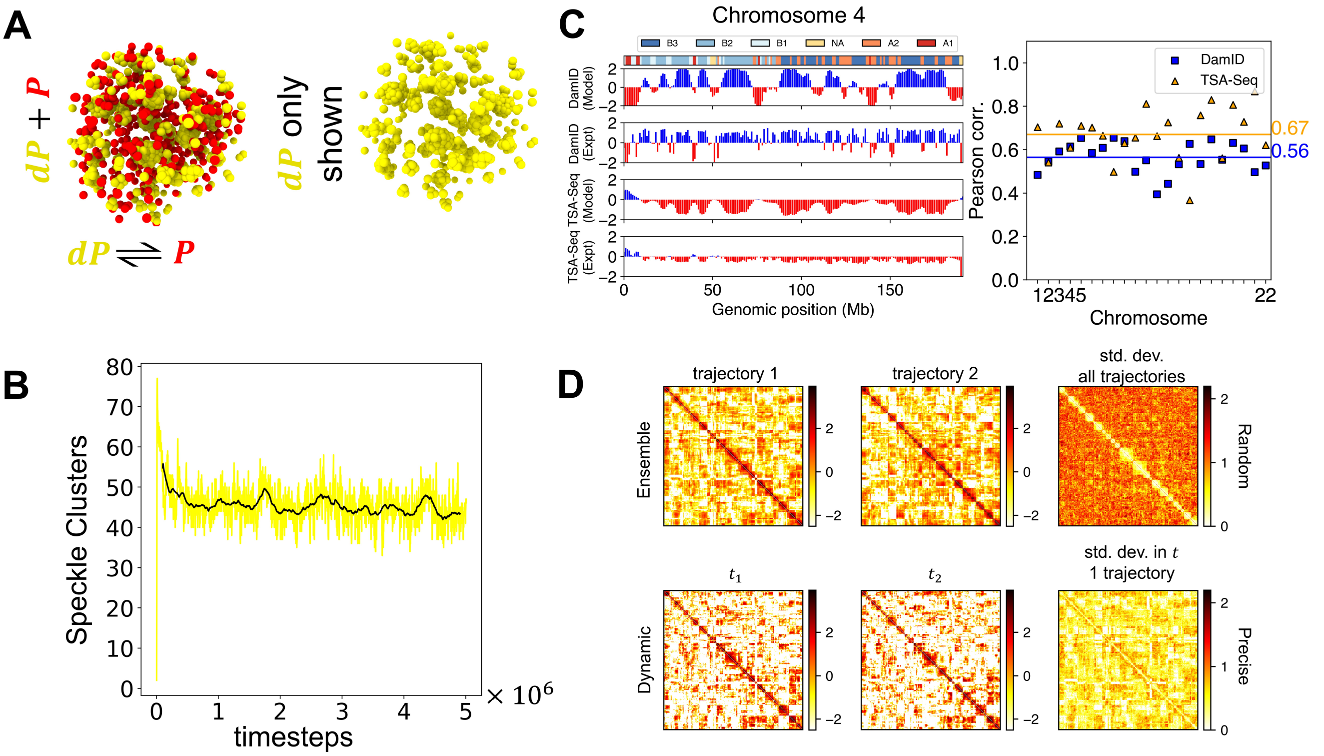

Figure S4: **Non-equilibrium speckle model.** (A) We developed an alternate model where we used semi-grand Monte Carlo to simulate chemical modifications within speckle particles. We ran simulations with two types of speckle particles (dephosphorylated and phosphorylated). The dP particles self assemble into speckle clusters while the constant exchange between dP and P particles stabilizes the individual clusters. (B) The number of speckle clusters as a function of the simulation timesteps. The dynamic fluctuations in the speckle number are achieved due to our kinetic scheme. (C) The sequencing predictions for Chromosome 4 are shown which are in good agreement with experimental data. Additionally the model predictions are similar to the one shown in Figure 3b of the main text. The genome-wide Pearson r correlation coefficient for agreement with sequencing experiments highlights the robustness of the model to the choice of speckle model parameters. (D) Contact maps were computed similarly as those presented in Figure 6 of the main text, but using genome structures from simulations of a non-equilibrium model for speckles. They demonstrate that incorporating a much more complex treatment of the speckle-speckle and speckle-chromatin interaction yields similar results as discussed in the main text.

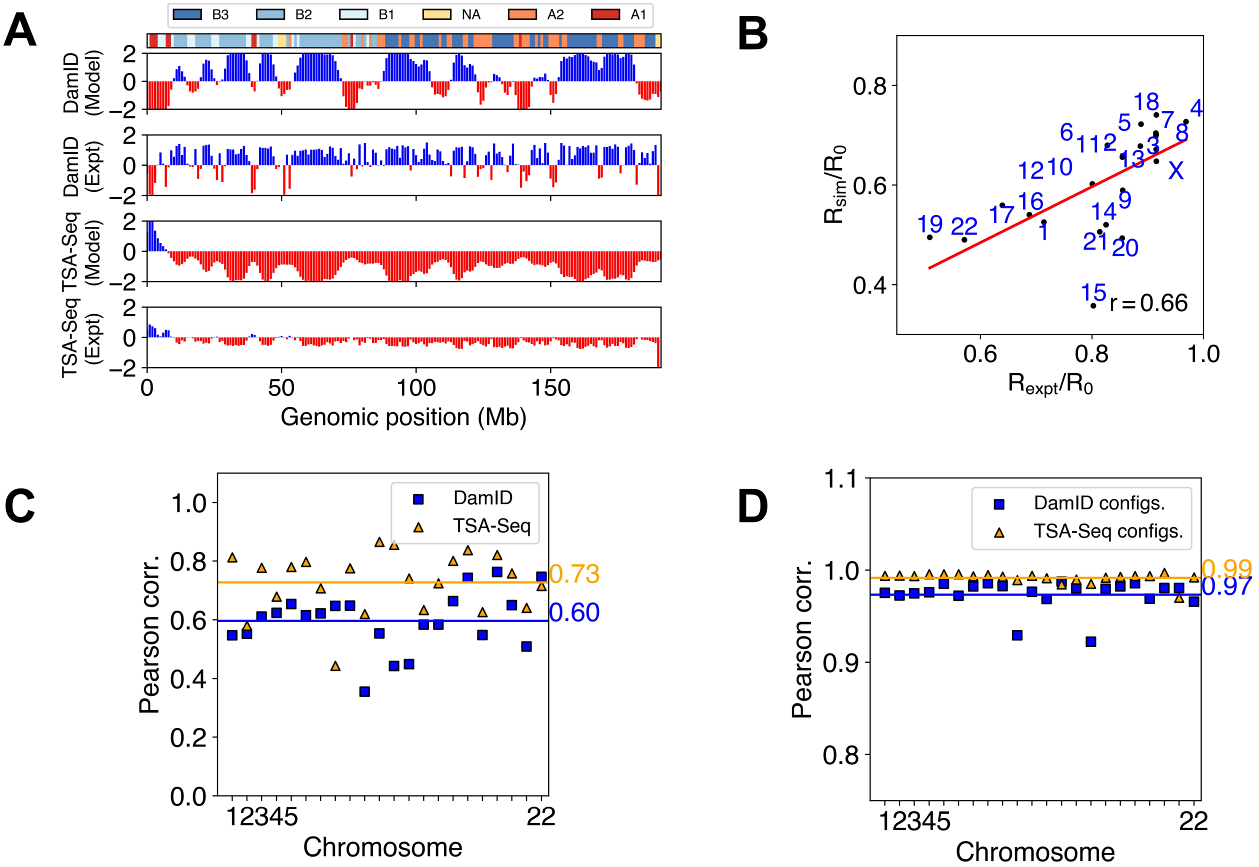

Figure S5: **Converged configurations are independent of initial conditions.** See text *Section: Initializing simulations with randomly places chromosomes* for simulation details. (A) The agreement with sequencing experiments (for chromosome 4) are shown for simulation started with random initial configurations. (B) The correlation between the simulated and experimental chromosome positions with random initial configurations is very similar to that obtained in Figure 4 of the main text. (C) The genome-wide agreement with sequencing experiments. (D) We calculated the Pearson r correlation between the DamID and TSA-Seq profiles for simulations with completely random configurations and with configurations initialised from a previous study.(22) Clearly, our simulations are well converged and our analysis is insensitive to the choice of the initial configurations.

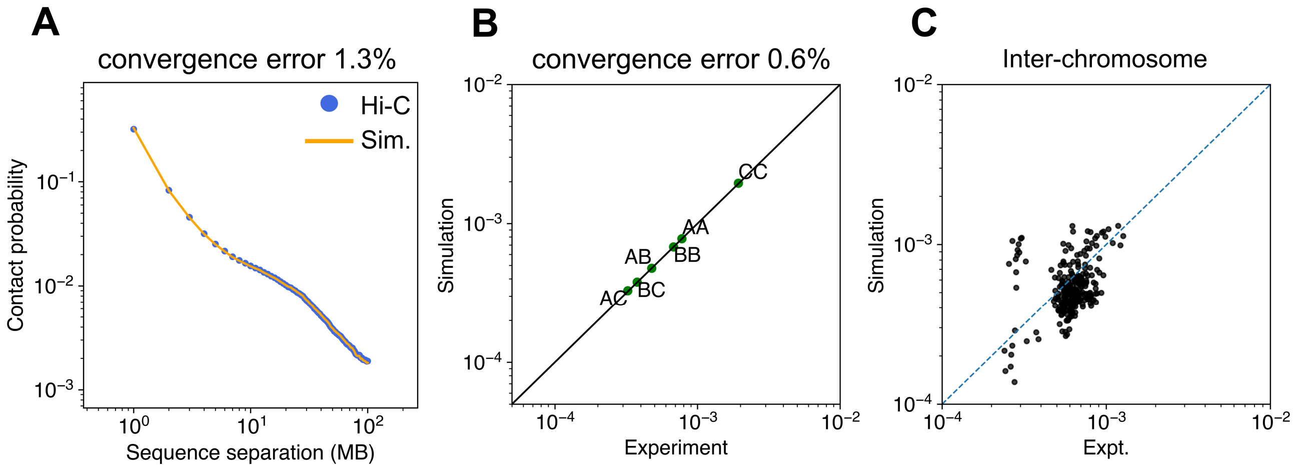

Figure S6: **Additional comparison of the model with Hi-C data.** (A) Power-law decay of the intra-chromosomal contact probability. The intra-chromosome contact probabilities in the model are optimized using the maximum entropy algorithm such that the model probabilities converge to the Hi-C contact probabilities. (B) The compartment-compartment interaction parameters in the model are optimized to match experimental contact probabilities and the resulting match is highlighted by the parity plot. (C) The model does not explicitly incorporate chromosome-specific interactions but yields a reasonable comparison with experimental inter-chromosome contact probabilities.

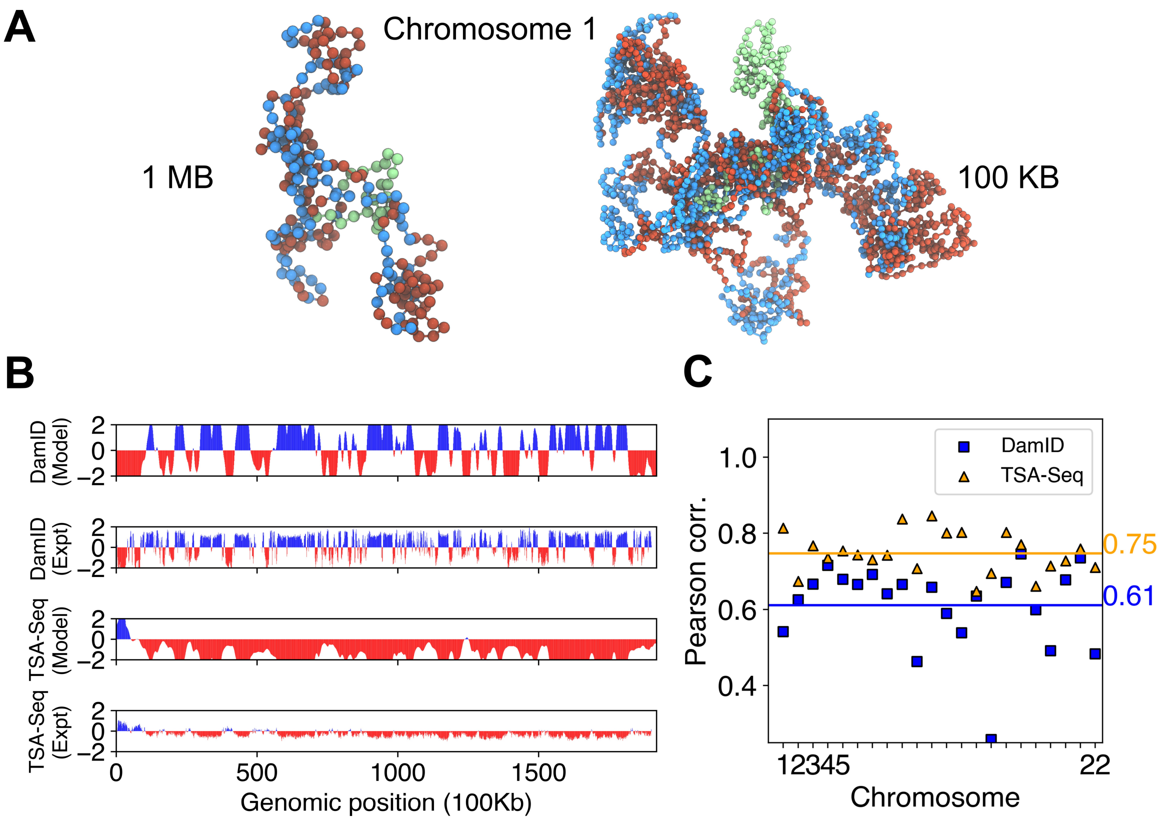

Figure S7: **Simulation results at the 100 kb resolution.** See text *Section: Modeling the genome at the 100 KB resolution* for simulation details and additional discussion. (A) Illustration of the increase in resolution of the model shown for Chromosome 1. (B) DamID and TSA-Seq profiles from the model compared against experiments at the 100kb resolution. (C) We observe a good genome wide agreement between model predictions and experimental sequencing profiles.

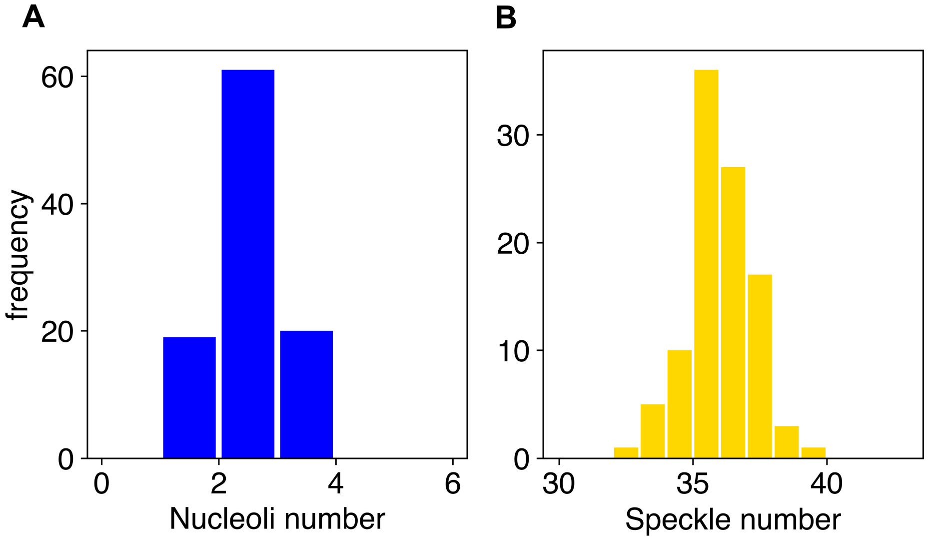

Figure S8: **Distribution of the number of nucleoli and speckles**. The average number (calculated from 100 independent trajectories) of nucleoli in our model is 2 and the average number of speckles in our model is 36.

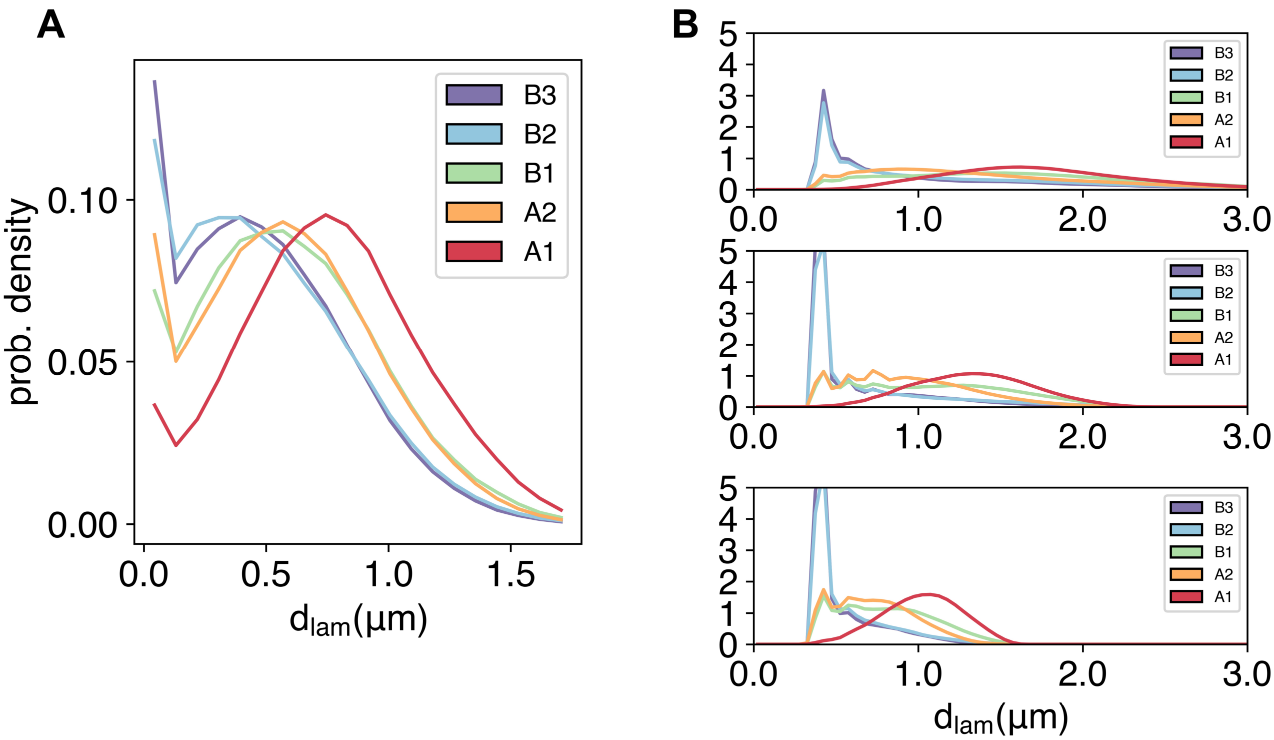

Figure S9: **Comparison between simulated and experimental distribution of genome subcompartments as a function of distance from nuclear lamina (d_{lam}).**. (A) Sensitivity of the experimental probability distribution at small distances with respect to the definition of nuclear envelope. The nuclear lamina was not explicitly imaged in Ref. 6. Instead, Su et. al used a convex hull algorithm to identify the outermost probes in their imaging assays as lamina. The important distinction here is that chromatin probes in their study that are exactly at a $d_{lam} = 0$ are defined as lamina and left out from subsequent analysis. However, including all the points that form the outermost portion of their convex hull reveals a peak in the distribution of B compartments at the periphery. (B) Sensitivity of the simulated probability distribution with respect to the shape of nuclear envelope. We carried out additional simulations with ellipsoidal shapes be setting the three semi-axes of the ellipsoid set as (10, 5, 2.5) μm and (15, 5, 1.67) μm, respectively. The corresponding results are shown in the middle and bottom panel, Compared to those shown in the main text (top panel), the range of values for the distance to lamina from various genomic regions gradually decrease and eventually reach values comparable to that seen in the experiment.

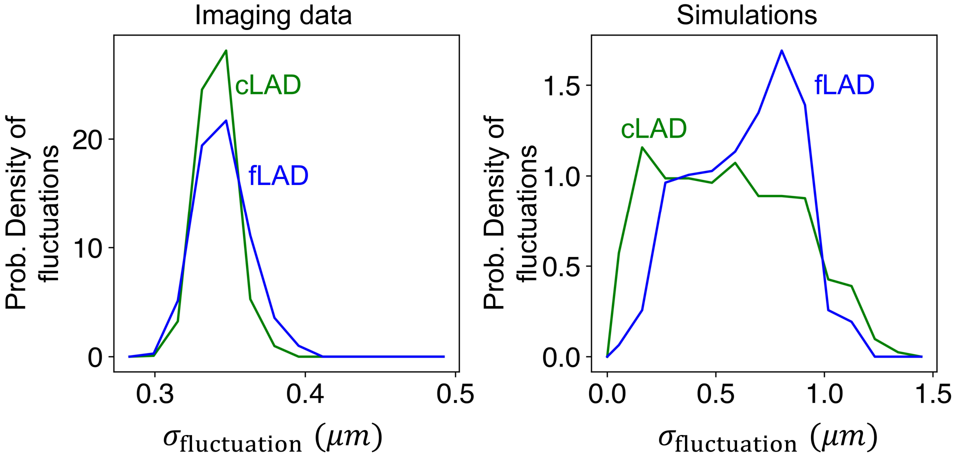

Figure S10: **The distribution of fluctuations in cLADs and fLADs in the imaging and simulation data.** $\sigma_{\text{fluctuation}}$ quantifies the variance of the distance to lamina among the two types of lamina-associated domains (LADs). The probability density plots were estimated using different cells from imaging (left) and different simulation trajectories (right). Consistent with the imaging data, our model predictions suggest that fLADs have a slightly higher fluctuation in distances from lamina compared to cLADs. See text *Section:Dynamical fluctuation of two different LADs* for additional discussion.

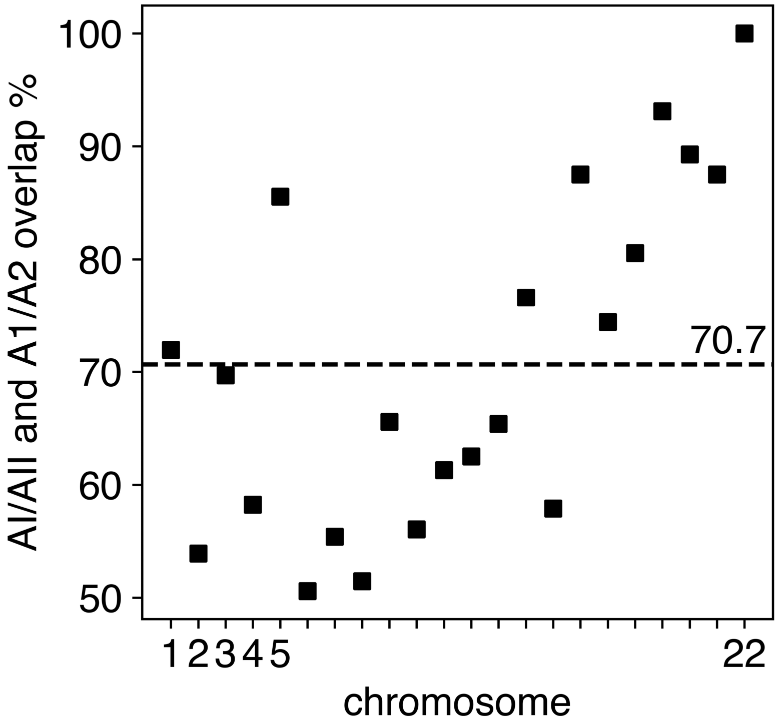

Figure S11: **Two A compartment sub-types obtained from clustering simulated genome-wide contact matrices compared with the experimental sub-compartment annotations.** The A subcompartments obtained from clustering the contact matrix are denoted as AI and AII (see Fig 5 of main text) and are in good agreement with the $A1$ and $A2$ inferred from subcompartment annotations. The genome-wide average overlap is 70.7%. See text *Section: Sub-compartment analysis of simulated contact maps* for more details on extracting AI and AII from simulated contact maps.

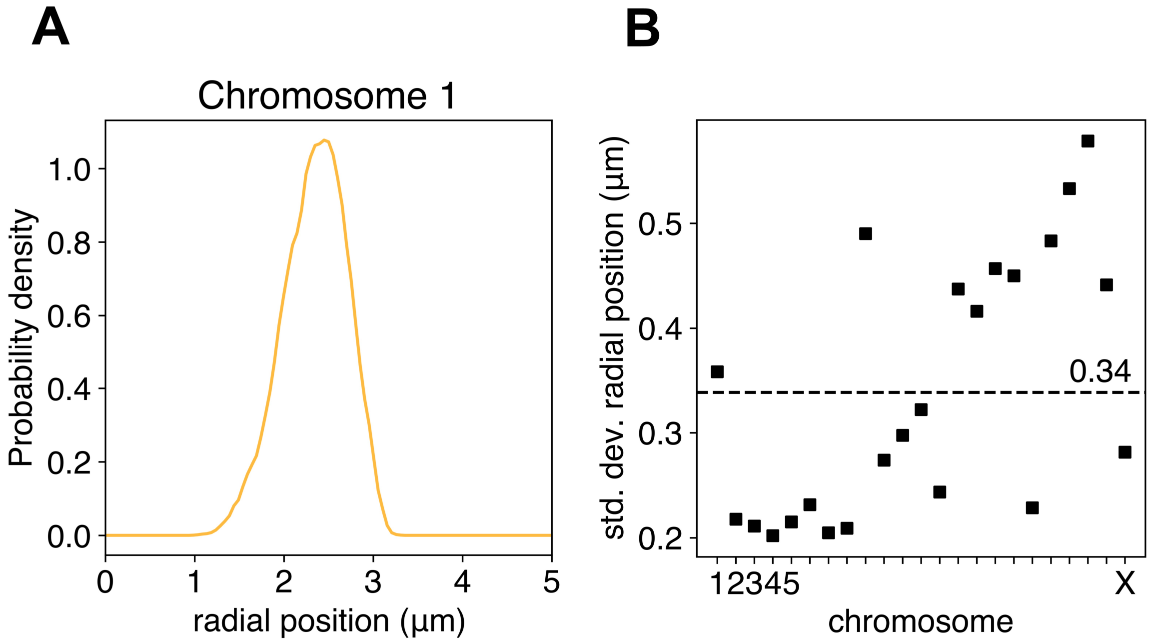

Figure S12: **Fluctuation in simulated chromosome positions.** (A) The distribution of chromosome 1 radial positions from simulations. (B) Standard deviations in radial position i.e. σ_r (in μm) of all chromosomes has a genome-wide average value of 0.34 μm. It is to be noted that on approximating the total spread of the distribution as $4\sigma_r$-$6\sigma_r$, the heterogeneity in radial positions 1.36-2.04 μm is fairly large.

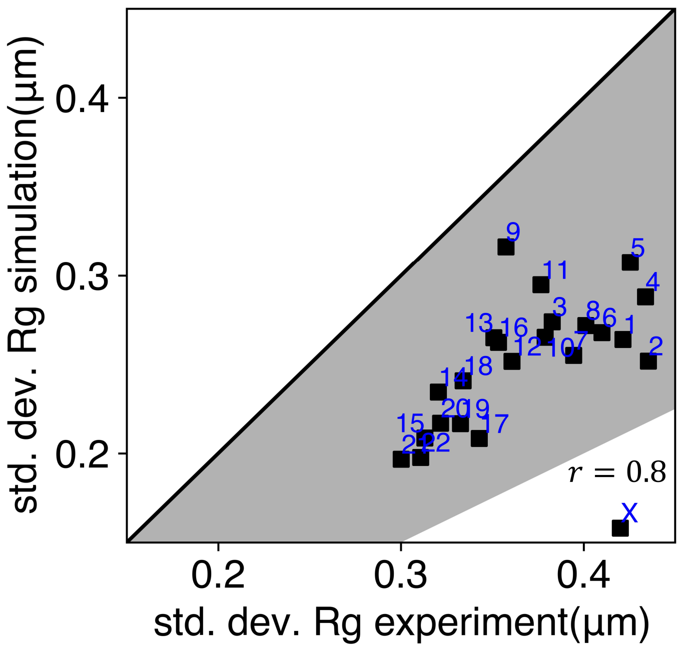

Figure S13: **Fluctuation of chromosome radius of gyration.** The standard deviations in radius of gyration distributions calculated from DNA-MERFISH experiments and our simulations is shown. We report the correlation coefficient on ignoring two outlier chromosomes (9 and X). The HFF cell is a male cell-type and we did not explicitly model the X and Y chromosomes differently which could be one of the reasons for chromosome X being a clear outlier. The black solid line is the parity line. Clearly, unlike the mean R_g (see Fig 4a of main text) the fluctuations in the simulations are not in perfect agreement with experiments. However, for almost all chromosomes the fluctuations are within a factor of two of the experiments as highlighted by the grey shaded region.

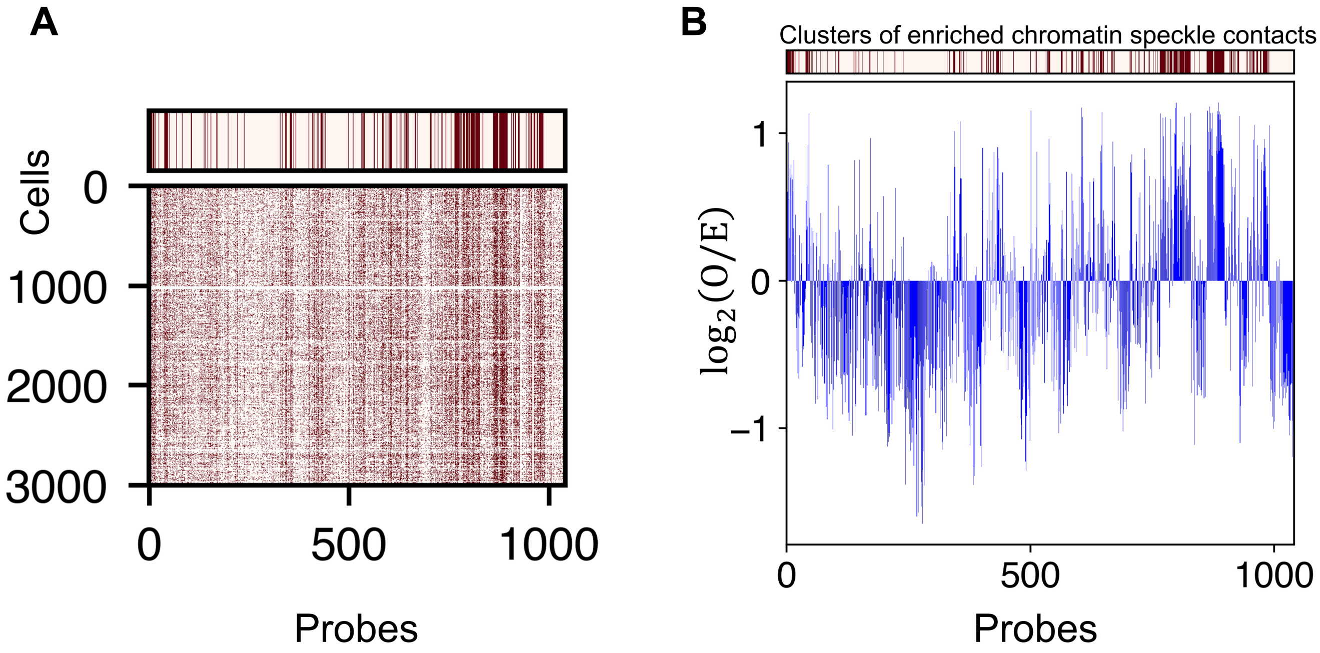

Figure S14: **Clustering chromatin-speckle contacts in the imaging data.** (A) Binary contact matrix for the imaging data with a speckle distance of probe less than $0.5\mu m$ defined as a contact. Clearly, some probes on the chromatin segments are more often in contact with speckles across different cells. We used K-means clustering to identify chromatin segments that are frequently in contact with the speckles. The clustered annotations are shown above the matrix. (B) The identified clusters line up well when compared against a segment-wise enrichment plot for speckle contacts. We use the cluster labels that are enriched in speckle contacts to compute the A1-A1 contact matrix discussed in Figure S15.

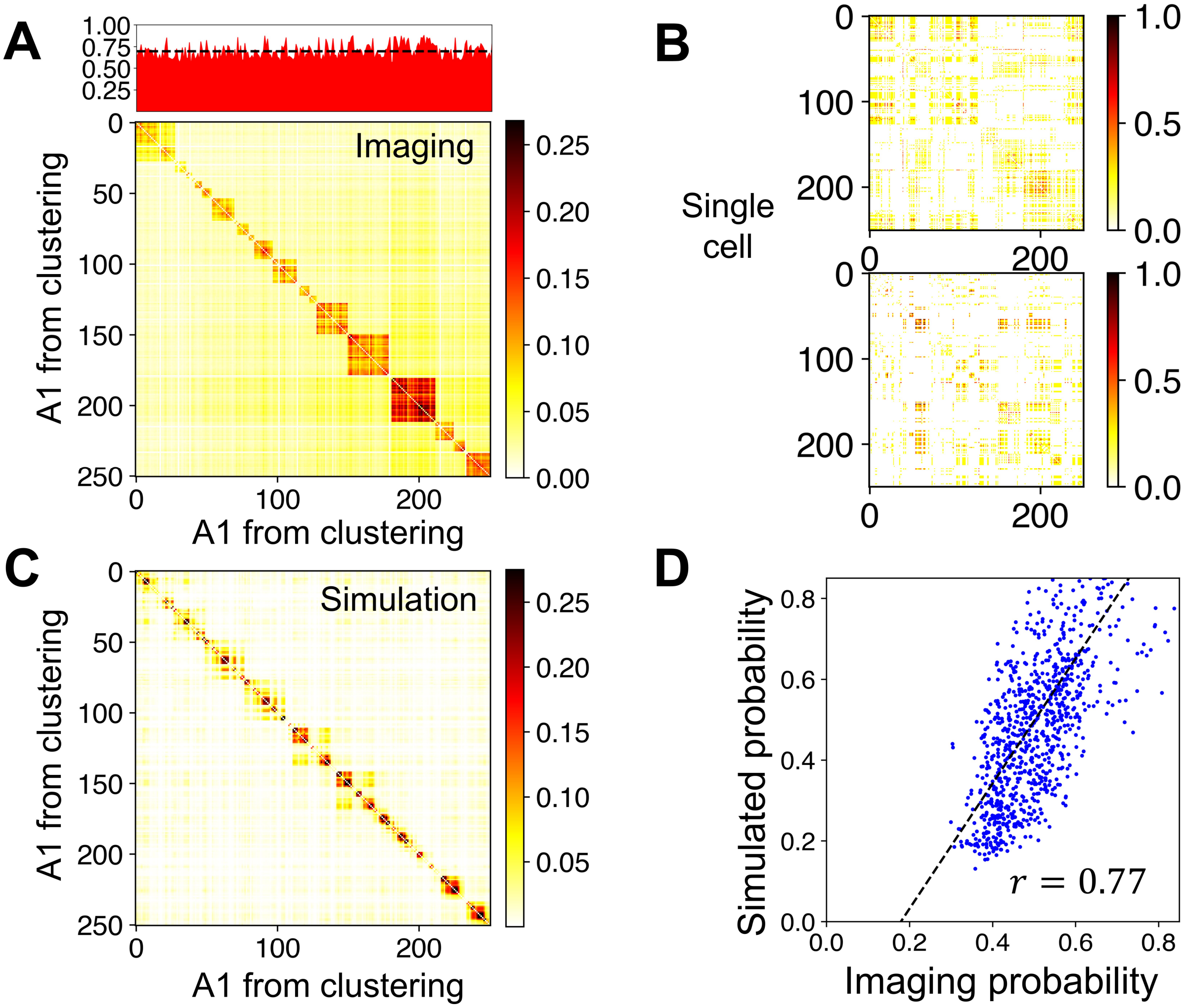

Figure S15: **Coexistence of heterogeneity and precision observed in imaging data** (A) The average A1-A1 contact matrix determined using DNA MERFISH imaging data. Contacts were defined only for pairs of chromatin segments bound to the same speckle, with the average probabilities across different cells ranges from 0-0.25. However, when we calculate the probability for the A1 segments to be in contact with speckles (see panel above the matrix) the contact probability is much higher as the segments are consistently in contact (with a mean value of 0.70) with speckles across different cells. (B) The contact matrix for individual single cells highlights the variability in contacts. (C) The average A1-A1 contact matrix from simulations for A1 segments identified using clustering strategy discussed in S14. We observed that this matrix is in good agreement with the matrix in Figure S15A with a Pearson correlation coefficient of 0.39. The less than perfect agreement between simulation and experimental results could arise from the difference in cell types, nucleus shape, and speckle numbers. Despite the complexity of cell nuclei, we found it encouraging that the average A1-A1 contact probabilities for the off diagonals (inter-chromosomal) is within a factor of 3.5 of the imaging data set. Therefore, the simulated genome ensemble provides a reliable representation of the structural heterogeneity of cell nuclei. (D) We compare the contact probability of all the chromatin segments (with speckles) in the DNA-MERFISH study with the chromatin-speckle contacts observed in our simulations. The high degree of correlation between the model and the experiment further validates the predictive capacity of the model.

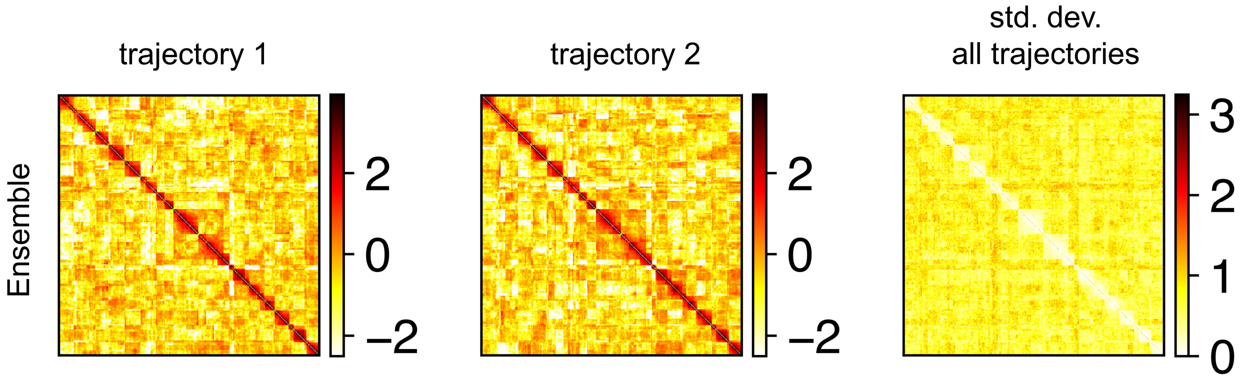

Figure S16: **Loss in heterogeneity between A1-A1 contacts upon removal of chromatin-speckle interactions**. See text *Perturbing chromatin-nuclear landmark interactions* for additional discussion. Contacts maps obtained from two independent trajectories (from different initial configurations) are shown in the left and middle panel. The standard deviation of contact maps obtained from 10 trajectories is shown in the right panel. Compared to Figure 6 of the main text, the difference in A1-A1 contact matrix (captured by the std. dev. matrix) is now much smaller.

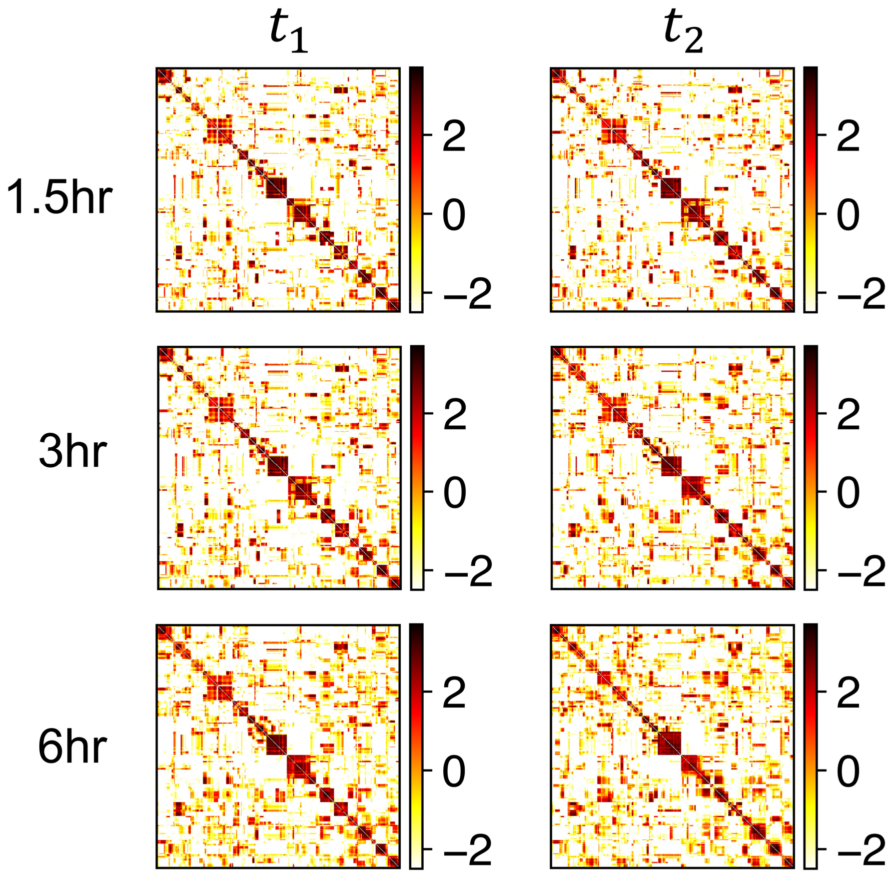

Figure S17: **A1-A1 contact matrix within a single trajectory.** The contacts between chromatin and speckles once formed have stable lifetimes across the time span of a single trajectory as observed in the structures generated from our model. We used the middle row for our results in Figure 6 of the main text. However, clearly the contact matrix is insensitive to the time difference over which the averages are computed because of the stability of the contacts within a trajectory.

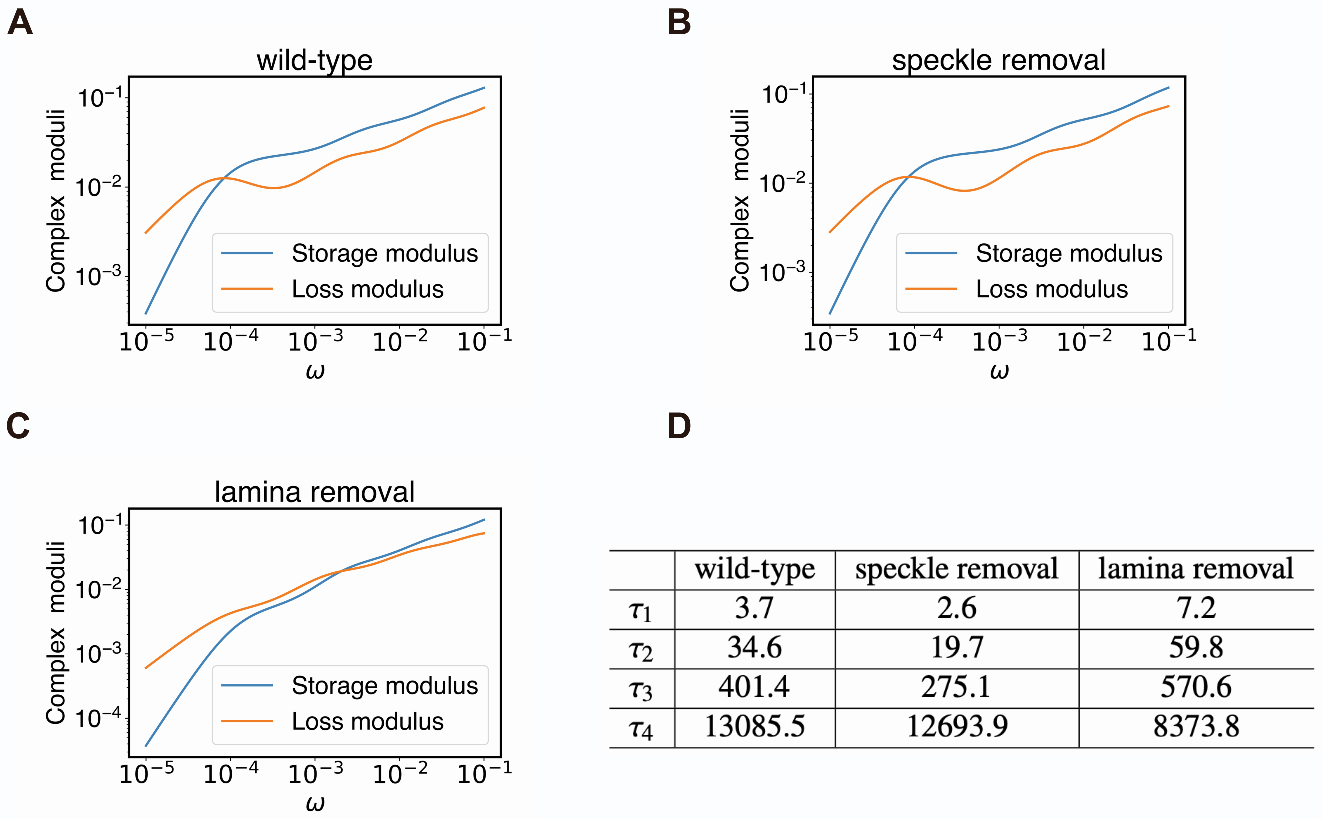

	wild-type	speckle removal	lamina removal
τ_1	3.7	2.6	7.2
τ_2	34.6	19.7	59.8
τ_3	401.4	275.1	570.6
τ_4	13085.5	12693.9	8373.8

Figure S18: **Complex modulus for the viscoelastic nuclear network.** See text *Section: Shear relaxation modulus of chromatin* for calculation details and *Section: Perturbing chromatin-nuclear landmark interactions: Chromatin-speckle interactions* for additional discussion. (A) Complex moduli for the 1 MB model developed in this study (wild-type). (B) Moduli for the system with abolished chromatin-speckle interactions. (C) Moduli for system with abolished chromatin-lamina interactions. (D) Timescale τ_n obtained by fitting Eq. S26 to $G(t)$ computed using simulations presented in the main text (wild type), simulations that removed chromatin-speckle interactions (speckle removal), and simulations removed chromatin-lamina interactions (lamina removal). The timescales are reported in reduced units.

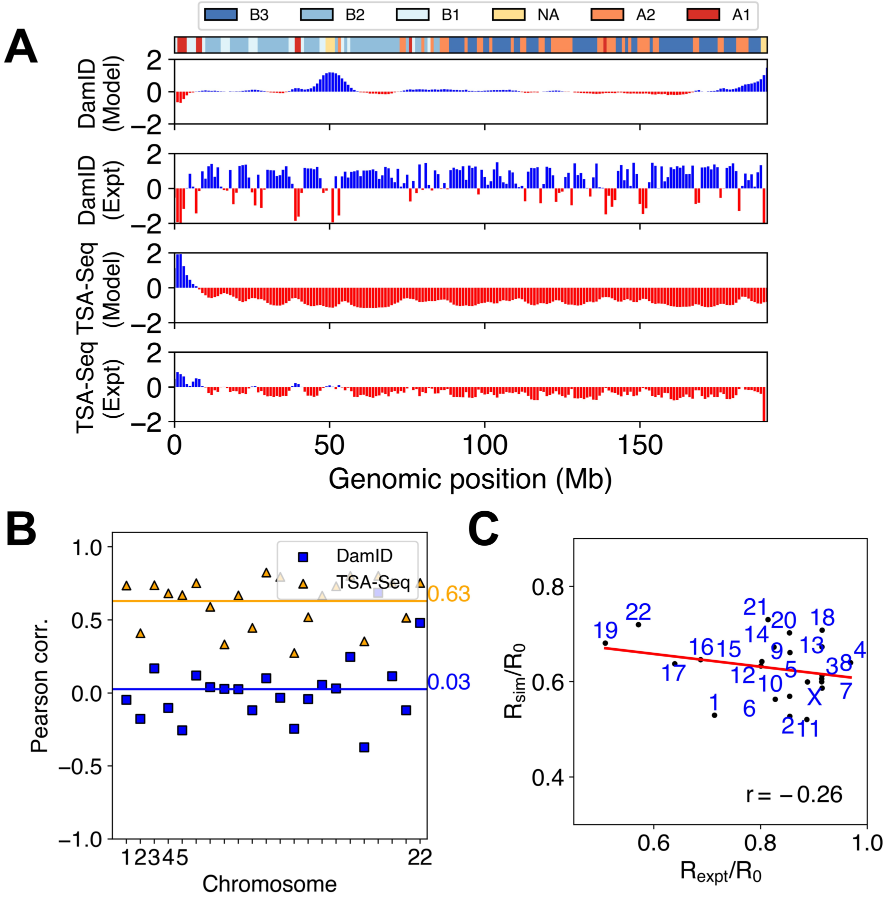

Figure S19: **Genome organization predicted by simulations that abolished chromatin-lamina interactions.** See text *Perturbing chromatin-nuclear landmark interactions* for additional discussion. (A) Comparison (for chromosome 4) between the model predicted Lamin-B DamID and SON TSA-Seq signals and the experimental data at 1MB resolution. (B) Pearson correlation coefficients between simulated and experimental Lamin-B DamID (blue) and SON TSA-Seq (yellow) data for individual chromosomes. The genome-wide averages are shown as straight lines with the corresponding values on the side. (C) Comparison of the chromosome radial positions in experiment (28) and simulations. Here R_0 is the radius of the nucleus and $R_0 = 13\sigma = 5\mu$m.

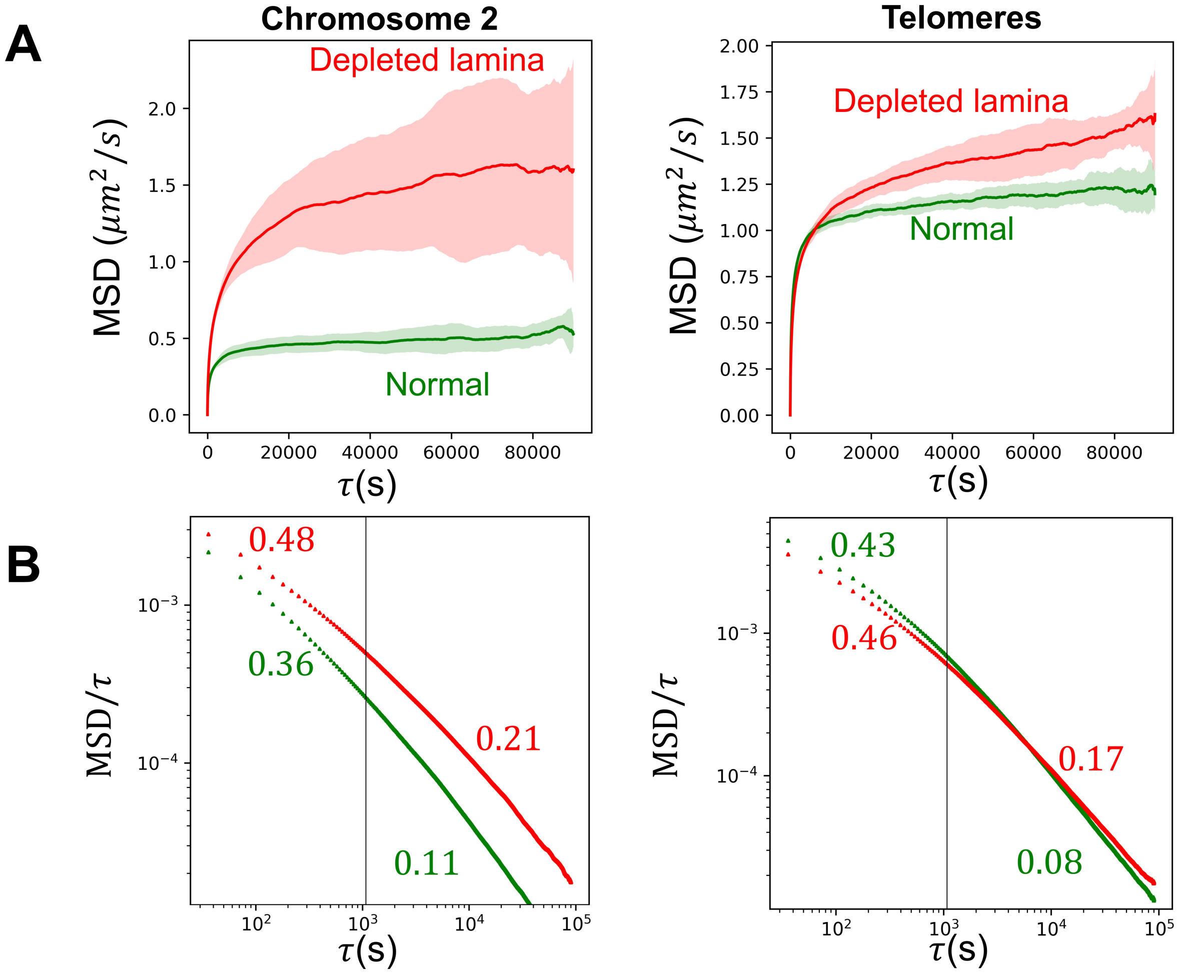

Figure S20: **Impact of chromatin-lamin interactions on the dynamics of genomic loci.** (A) The green curve is the mean square displacement (MSD) for Chromosome 2 and Telomeres averaged across 10 trajectories for the normal model. The error bars associated with the MSD is shown as a transparent region in green. Similarly, the MSD on zeroing the interaction between chromatin-lamina in the model (across 10 trajectories) is shown as red curves. Consistent with the Lamina depletion results of Chang et al., we see a pronounced effect on the dynamics of Chromosome 2 compared to the Telomeres.(16) (B) To further investigate the sub-diffusive exponent we performed careful analysis of the MSD data consistent with the procedure outlined by Bronshtein et al.(20). We converted the MSD vs τ data to MSD/τ vs τ data as the slope of log(MSD/τ) vs log(τ) is $\alpha - 1$ where α is exponent of the sub-diffusion process. Additionally, to estimate an average non-anomalous diffusion coefficient (in units of $\mu m^2/s$) we fit a linear line to the MSD data (skipping the first $3.6 \times 10^4 s$) We observe two regimes in the diffusion behavior (analysis boundary marked by the vertical solid black line). The exponents (α where MSD $\sim \tau^{\alpha}$) for the two regimes in the normal (green) and depleted (red) models are reported in the figure.

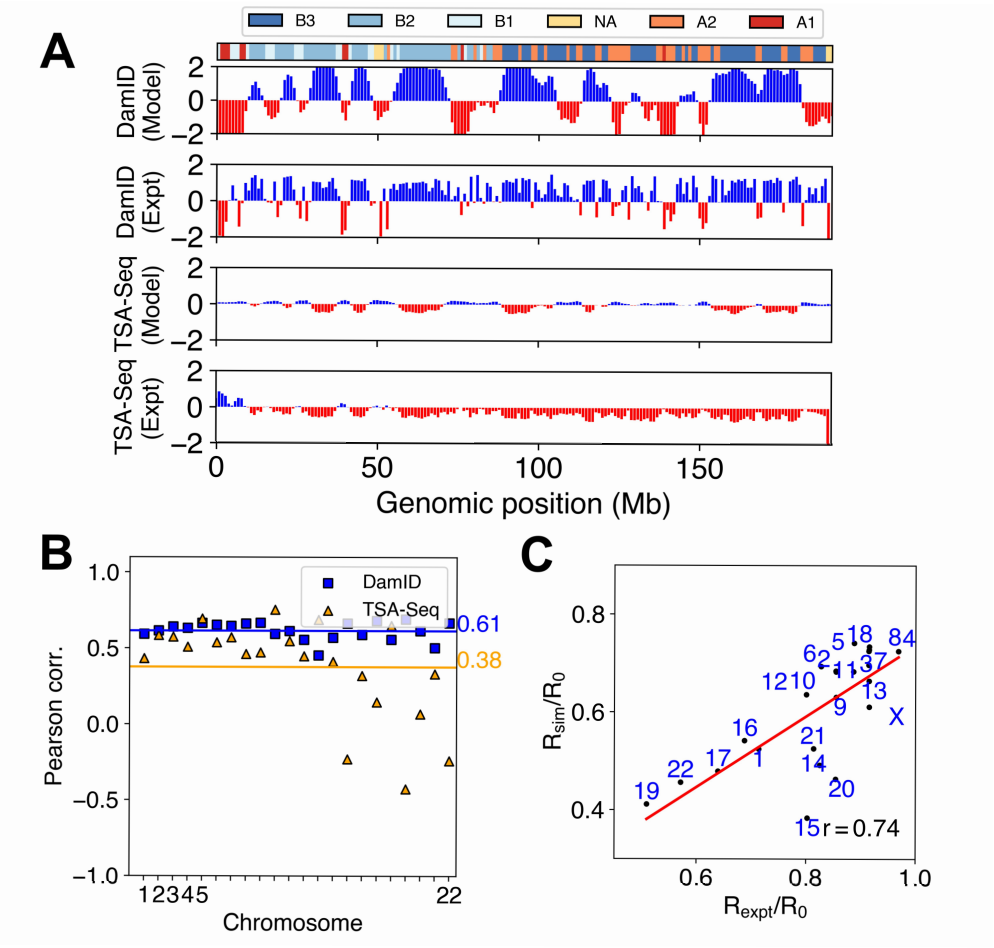

Figure S21: **Genome organization predicted by simulations that abolished chromatin-speckle interactions.** See text *Perturbing chromatin-nuclear landmark interactions* for additional discussion. (A) Comparison (for chromosome 4) between the model predicted Lamin-B DamID and SON TSA-Seq signals and the experimental data at 1MB resolution. (B) Pearson correlation coefficients between simulated and experimental Lamin-B DamID (blue) and SON TSA-Seq (yellow) data for individual chromosomes. The genome-wide averages are shown as straight lines with the corresponding values on the side. (C) Comparison of the chromosome radial positions in experiment (28) and simulations. Here R_0 is the radius of the nucleus and $R_0 = 13\sigma = 5\mu\text{m}$.

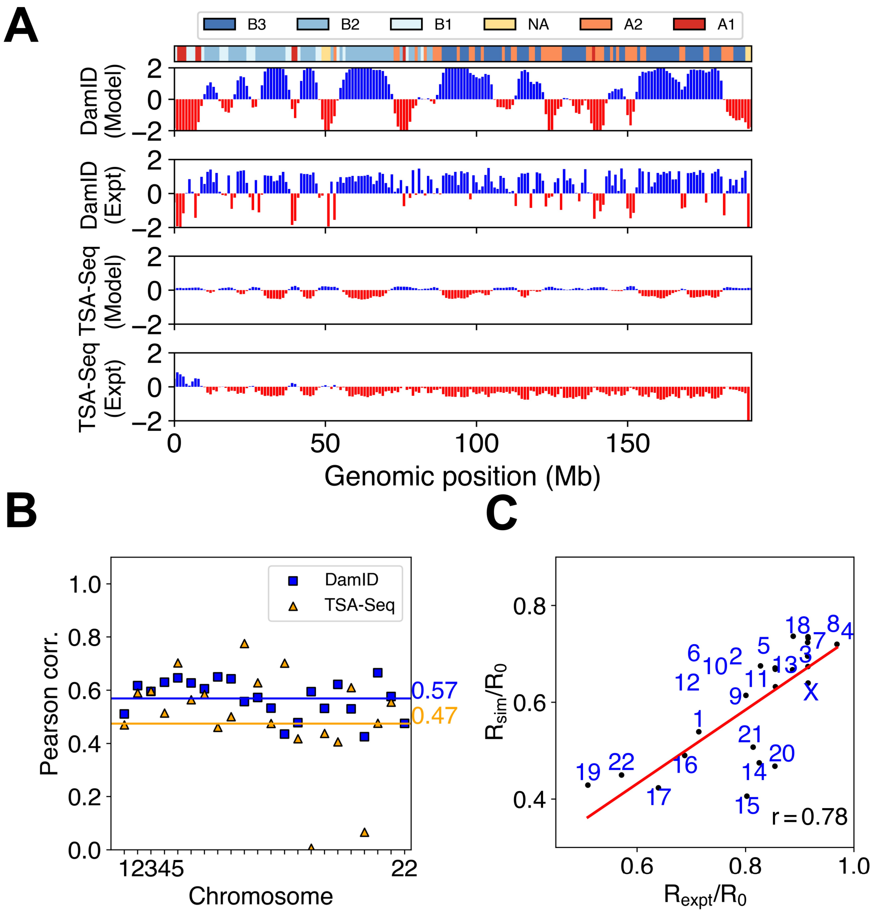

Figure S22: **Perturbing chromatin-speckle together with compartment interactions.** See text *Perturbing chromatin-nuclear landmark interactions* for additional discussion. (A) Comparison (for chromosome 4) between the model predicted Lamin-B DamID and SON TSA-Seq signals and the experimental data at 1MB resolution. (B) The model's ability to replicate TSA-Seq profiles has diminished significantly while the agreement with DamID profiles reduces slightly. (C) Although the model does not have chromatin-speckle and compartment-compartment interactions, the model preserves its capacity to replicate experimental radial positions.(28)

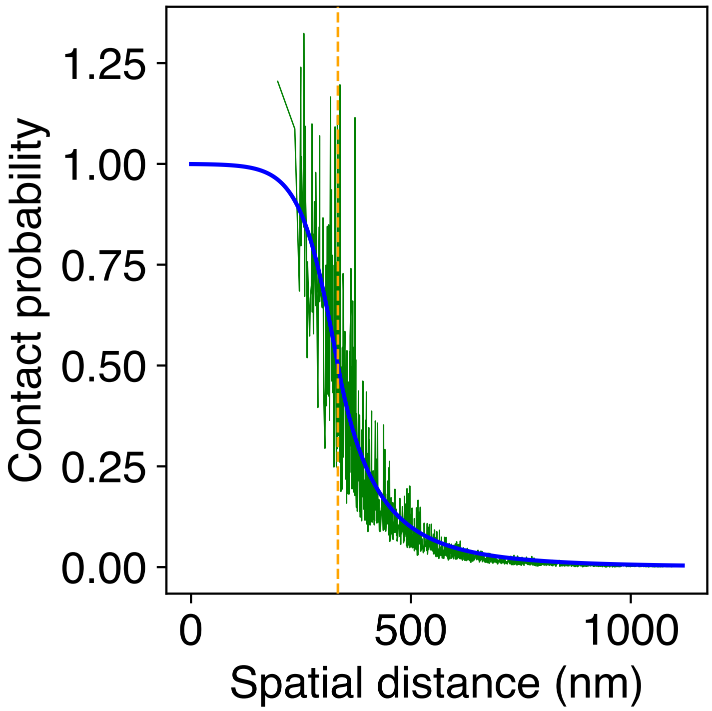

Figure S23: **Parameterizing contact function in the model using DNA-MERFISH imaging data.** The green solid lines are the raw contact probabilities from the imaging study. The blue solid line is the curve fit contact function (used in our model) that switches from a tanh function to a power law (as described by equation S10) at 334 nm (shown by the dashed orange line).

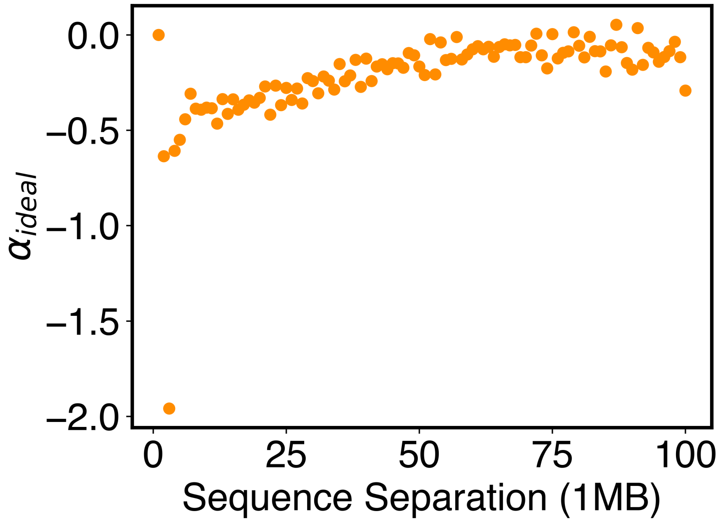

Figure S24: **Parameters in the ideal potential, $\alpha_{\textbf{ideal}}$, as defined in Eq. S9 as a function sequence separation.** See *Section:Hi-C inspired interactions for the diploid human genome* for more text on the definition of the potential and its parameterization from Hi-C data.

REFERENCES

1. Hetzer, M. W., 2010. The nuclear envelope. *Cold Spring Harbor perspectives in biology* 2:a000539.
2. Swinbank, R., and R. J. Purser, 2006. Fibonacci grids: A novel approach to global modelling. *Quarterly Journal of the Royal Meteorological Society* 132:1769–1793.
3. Li, C., A. Ji, and Z. Cao, 2007. Stressed Fibonacci spiral patterns of definite chirality. *Applied Physics Letters* 90:164102.
4. Qi, Y., and B. Zhang, 2021. Chromatin network retards nucleoli coalescence. *Nature communications* 12:1–10.
5. Handwerger, K. E., J. A. Cordero, and J. G. Gall, 2005. Cajal bodies, nucleoli, and speckles in the Xenopus oocyte nucleus have a low-density, sponge-like structure. *Molecular biology of the cell* 16:202–211.
6. Su, J.-H., P. Zheng, S. S. Kinrot, B. Bintu, and X. Zhuang, 2020. Genome-scale imaging of the 3D organization and transcriptional activity of chromatin. *Cell* 182:1641–1659.
7. Wang, Y., Y. Zhang, R. Zhang, T. van Schaik, L. Zhang, T. Sasaki, D. Peric-Hupkes, Y. Chen, D. M. Gilbert, B. van Steensel, A. S. Belmont, and J. Ma, 2021. SPIN reveals genome-wide landscape of nuclear compartmentalization. *Genome Biol.* 22:36.
8. Brackley, C. A., J. Johnson, D. Michieletto, A. N. Morozov, M. Nicodemi, P. R. Cook, and D. Marenduzzo, 2017. Nonequilibrium chromosome looping via molecular slip links. *Physical review letters* 119:138101.
9. Nomidis, S. K., E. Carlon, S. Gruber, and J. F. Marko, 2022. DNA tension-modulated translocation and loop extrusion by SMC complexes revealed by molecular dynamics simulations. *Nucleic Acids Research* 50:4974–4987.
10. Hughes, S. E., and R. S. Hawley, 2009. Heterochromatin: a rapidly evolving species barrier. *PLoS Biology* 7:e1000233.
11. Yukawa, H., 1935. On the interaction of elementary particles. I. *Proceedings of the Physico-Mathematical Society of Japan. 3rd Series* 17:48–57.
12. Farley, K. I., Y. Surovtseva, J. Merkel, and S. J. Baserga, 2015. Determinants of mammalian nucleolar architecture. *Chromosoma* 124:323–331.
13. Spector, D. L., and A. I. Lamond, 2011. Nuclear speckles. *Cold Spring Harb. Perspect. Biol.* 3:1–12.
14. Ugarte, F., R. Sousae, B. Cinquin, E. W. Martin, J. Krietsch, G. Sanchez, M. Inman, H. Tsang, M. Warr, E. Passegué, C. A. Larabell, and E. C. Forsberg, 2015. Progressive chromatin condensation and H3K9 methylation regulate the differentiation of embryonic and hematopoietic stem cells. *Stem Cell Reports* 5:728–740.
15. Johnstone, S. E., A. Reyes, Y. Qi, C. Adriaens, E. Hegazi, K. Pelka, J. H. Chen, L. S. Zou, Y. Drier, V. Hecht, N. Shoresh, M. K. Selig, C. A. Lareau, S. Iyer, S. C. Nguyen, E. F. Joyce, N. Hacohen, R. A. Irizarry, B. Zhang, M. J. Aryee, and B. E. Bernstein, 2020. Large-Scale Topological Changes Restrain Malignant Progression in Colorectal Cancer. *Cell* 182:1474–1489.
16. Chang, L., M. Li, S. Shao, C. Li, S. Ai, B. Xue, Y. Hou, Y. Zhang, R. Li, X. Fan, A. He, C. Li, and Y. Sun, 2022. Nuclear peripheral chromatin-lamin B1 interaction is required for global integrity of chromatin architecture and dynamics in human cells. *Protein Cell* 13:258–280.
17. Jiang, Z., Y. Qi, K. Kamat, and B. Zhang, 2022. Phase Separation and Correlated Motions in Motorized Genome. *J. Phys. Chem. B* `https://pubs.acs.org/doi/10.1021/acs.jpcb.2c03238`.
18. Amendola, M., and B. Steensel, 2015. Nuclear lamins are not required for lamina-associated domain organization in mouse embryonic stem cells. *EMBO Rep.* 16:610–617.
19. Zheng, X., J. Hu, S. Yue, L. Kristiani, M. Kim, M. Sauria, J. Taylor, Y. Kim, and Y. Zheng, 2018. Lamins Organize the Global Three-Dimensional Genome from the Nuclear Periphery. *Mol. Cell* 71:802–815.e7. `https://doi.org/10.1016/j.molcel.2018.05.017`.
20. Bronshtein, I., E. Kepten, I. Kanter, S. Berezin, M. Lindner, A. B. Redwood, S. Mai, S. Gonzalo, R. Foisner, Y. Shav-Tal, and Y. Garini, 2015. Loss of lamin A function increases chromatin dynamics in the nuclear interior. *Nat. Commun.* 6:8044. `http://dx.doi.org/10.1038/ncomms9044http://www.nature.com/articles/ncomms9044`.

21. Kumaran, R. I., B. Muralikrishna, and V. K. Parnaik, 2002. Lamin A/C speckles mediate spatial organization of splicing factor compartments and RNA polymerase II transcription. *J. Cell Biol.* 159:783–793.

22. Qi, Y., A. Reyes, S. E. S. Johnstone, M. M. J. Aryee, B. B. E. Bernstein, and B. Zhang, 2020. Data-Driven Polymer Model for Mechanistic Exploration of Diploid Genome Organization. *Biophys. J.* 119:1905–1916. `https://linkinghub.elsevier.com/retrieve/pii/S0006349520307190`.

23. Carrero, G., M. Hendzel, and G. De Vries, 2006. Modelling the compartmentalization of splicing factors. *Journal of theoretical biology* 239:298–312.

24. Velazquez-Dones, A., J. C. Hagopian, C.-T. Ma, X.-Y. Zhong, H. Zhou, G. Ghosh, X.-D. Fu, and J. A. Adams, 2005. Mass spectrometric and kinetic analysis of ASF/SF2 phosphorylation by SRPK1 and Clk/Sty. *Journal of Biological Chemistry* 280:41761–41768.

25. Ester, M., H.-P. Kriegel, J. Sander, X. Xu, et al., 1996. A density-based algorithm for discovering clusters in large spatial databases with noise. *In* kdd. volume 96, 226–231.

26. Chen, Y., Y. Zhang, Y. Wang, L. Zhang, E. K. Brinkman, S. A. Adam, R. Goldman, B. Van Steensel, J. Ma, and A. S. Belmont, 2018. Mapping 3D genome organization relative to nuclear compartments using TSA-Seq as a cytological ruler. *Journal of Cell Biology* 217:4025–4048.

27. Rao, S. S., M. H. Huntley, N. C. Durand, E. K. Stamenova, I. D. Bochkov, J. T. Robinson, A. L. Sanborn, I. Machol, A. D. Omer, E. S. Lander, and E. L. Aiden, 2014. A 3D map of the human genome at kilobase resolution reveals principles of chromatin looping. *Cell* 159:1665–1680. `http://www.sciencedirect.com/science/article/pii/S0092867414014974`.

28. Boyle, S., S. Gilchrist, J. M. Bridger, N. L. Mahy, J. Ellis, and W. A. Bickmore, 2001. The spatial organization of human chromosomes within the nuclei of normal and emerin-mutant cells. *Hum. Mol. Genet.* 10:211–219. `https://academic.oup.com/hmg/article-lookup/doi/10.1093/hmg/10.3.211`.